



Reprogramming exosomes for immunity-remodeled photodynamic therapy against non-small cell lung cancer

Jiao Guo^{a,1}, Wei Zhao^{a,1}, Xinyu Xiao^a, Shanshan Liu^b, Liang Liu^a, La Zhang^c, Lu Li^a, Zhenghang Li^d, Zhi Li^e, Mengxia Xu^e, Qiling Peng^{a,f,g,**}, Jianwei Wang^{a,***}, Yuxian Wei^{d,****}, Ning Jiang^{h,i,j,*}

^a School of Basic Medical Science, Chongqing Medical University, Chongqing, 400016, China

^b Department of Plastic and Maxillofacial Surgery, The Second Affiliated Hospital of Chongqing Medical University, Chongqing, 400016, China

^c Department of Hepatobiliary Surgery, The First Affiliated Hospital of Chongqing Medical University, Chongqing, 400016, China

^d Department of Breast and Thyroid Surgery, The First Affiliated Hospital of Chongqing Medical University, Chongqing, 400016, China

^e Traditional Chinese Medicine Hospital of Bijie City, Guizhou province, 551700, China

^f Bijie Municipal Health Bureau, Guizhou province, 551700, China

^g Health Management Center, the Affiliated Hospital of Guizhou Medical University

^h Department of Pathology, School of Basic Medical Science, Chongqing Medical University, Chongqing, 400016, China

ⁱ Molecular Medicine Diagnostic and Testing Center, Chongqing Medical University, Chongqing, 400016, China

^j Department of Pathology, The First Affiliated Hospital of Chongqing Medical University, Chongqing, 400016, China

ARTICLE INFO

Keywords:

Non-small cell lung cancer
PDT
Immunotherapy
Tumor microenvironment
PD-L1
Targeted delivery

ABSTRACT

Traditional treatments against advanced non-small cell lung cancer (NSCLC) with high morbidity and mortality continue to be dissatisfactory. Given this situation, there is an urgent requirement for alternative modalities that provide lower invasiveness, superior clinical effectiveness, and minimal adverse effects. The combination of photodynamic therapy (PDT) and immunotherapy gradually become a promising approach for high-grade malignant NSCLC. Nevertheless, owing to the absence of precise drug delivery techniques as well as the hypoxic and immunosuppressive characteristics of the tumor microenvironment (TME), the efficacy of this combination therapy approach is less than ideal. In this study, we construct a novel nanoplatform that indocyanine green (ICG), a photosensitizer, loads into hollow manganese dioxide (MnO₂) nanospheres (NPs) (ICG@MnO₂), and then encapsulated in PD-L1 monoclonal antibodies (anti-PD-L1) reprogrammed exosomes (named ICG@MnO₂@Exo-anti-PD-L1), to effectively modulate the TME to oppose NSCLC by the synergy of PDT and immunotherapy modalities. The ICG@MnO₂@Exo-anti-PD-L1 NPs are precisely delivered to the tumor sites by targeting specially PD-L1 highly expressed cancer cells to controllably release anti-PD-L1 in the acidic TME, thereby activating T cell response. Subsequently, upon endocytic uptake by cancer cells, MnO₂ catalyzes the conversion of H₂O₂ to O₂, thereby alleviating tumor hypoxia. Meanwhile, ICG further utilizes O₂ to produce singlet oxygen (¹O₂) to kill tumor cells under 808 nm near-infrared (NIR) irradiation. Furthermore, a high level of intratumoral H₂O₂ reduces MnO₂ to Mn²⁺, which remodels the immune microenvironment by polarizing macrophages from M2 to M1, further driving T cells. Taken together, the current study suggests that the ICG@MnO₂@Exo-anti-PD-L1 NPs could act as a novel drug delivery platform for achieving multimodal therapy in treating NSCLC.

Peer review under responsibility of KeAi Communications Co., Ltd.

* Corresponding author.

** Corresponding author.

*** Corresponding author.

**** Corresponding author.

E-mail addresses: pqlpzy@cqmu.edu.cn (Q. Peng), jianweiwangcn@cqmu.edu.cn (J. Wang), weiyuxian@cqmu.edu.cn (Y. Wei), jiangning@cqmu.edu.cn (N. Jiang).

¹ These authors contributed equally to this work.

<https://doi.org/10.1016/j.bioactmat.2024.05.030>

Received 2 November 2023; Received in revised form 11 April 2024; Accepted 16 May 2024

2452-199X/© 2024 The Authors. Publishing services by Elsevier B.V. on behalf of KeAi Communications Co. Ltd. This is an open access article under the CC BY-NC-ND license (<http://creativecommons.org/licenses/by-nc-nd/4.0/>).

1. Introduction

Lung cancer, one of the most prevalent malignancies worldwide, stands as the foremost contributor to cancer-related mortality with an alarming incidence of over 2.2 million new cases reported in the Global Cancer Statistics 2020 [1]. Remarkably, non-small cell lung cancer (NSCLC) constitutes around 85 % of all lung cancer cases [2,3], and it is associated with a grim prognosis, having a five-year survival rate of less than 18 % [4]. NSCLC encompasses various types of epithelial lung cancers, such as squamous cell carcinoma, large cell carcinoma, and adenocarcinoma, while excluding small cell lung cancer (SCLC) [5]. At present, the conventional treatment options for NSCLC include surgery, radiotherapy, chemotherapy, targeted therapy, and immunotherapy [6, 7]. Surgery is the usual primary treatment for early-stage NSCLC [8], but around 40 % of NSCLC patients are diagnosed at stage IV, thereby precluding them from undergoing surgical intervention [9]. Radiotherapy and platinum-based chemotherapy are the main treatments for these advanced NSCLC [10,11]. Nevertheless, due to tumor drug resistance, severe side effects and the deficiency of drug-targeted delivery, the effectiveness of radiotherapy and chemotherapy is significantly compromised [12,13]. Hence, it is of great medical and social value to explore novel therapeutic strategies for NSCLC to surpass the constraints of traditional treatment approaches and attain improved outcomes.

Photodynamic therapy (PDT) is gradually gaining attention and application in the field of cancer treatment, boasting qualities such as minimally invasive procedures, high selectivity, low toxicity, and reusability [14]. Increasing researches recommend PDT for the treatment of lung cancer, including NSCLC [15,16]. PDT represents a novel modality to anti-cancer treatment, which utilizes photosensitizers to generate reactive oxygen species (ROS) from molecular oxygen (O_2) when exposed to light, resulting in the selective eradication of tumor cells through oxidative damage to DNA, lipids, and proteins, and ultimately inducing tumor cells death [14,17]. It has been demonstrated that hypoxia is one of the most important features of the solid tumor microenvironment (TME), being implicated in tumor invasion, immune escape, metastasis, and resistance to PDT [18,19]. Interestingly, the TME exhibits a high concentration of hydrogen peroxide (H_2O_2), approximately 100 μM [20]. Therefore, a promising strategy for carcinoma therapy involves replenishing O_2 by harnessing endogenous H_2O_2 within the TME, thereby enhancing O_2 -dependent PDT efficiency and alleviating hypoxia-related issues. Manganese dioxide (MnO_2), as a unique and novel therapeutic agent, has garnered significant attention [21,22]. MnO_2 possesses the ability to catalytically decompose H_2O_2 present in the TME into H_2O and O_2 , thereby alleviating tumor hypoxia [23]. Furthermore, MnO_2 is reduced to harmless water-soluble Mn^{2+} that is rapidly excreted through the kidneys [24]. And that means MnO_2 exhibits low long-term toxicity. Meanwhile, an interesting observation is made that Mn^{2+} can remodel the immune microenvironment by inducing a shift of macrophages from M2 to M1 [25], which successively enhances the activation of T cells [26,27]. However, most of the previously reported MnO_2 nanospheres (NPs) may not efficiently achieve optimal drug loading and precisely controlled release, leading to sub-optimal therapeutic efficacy [28,29]. According to the literature, indocyanine green (ICG) is an FDA-approved drug with good biocompatibility and can be used as a photosensitizer in PDT [30], but owing to the short half-life in vivo and the lack of the specifically targeted capacity [31], its application in the field of PDT is limited. Based on the aforementioned challenges, the focus of this study is to explore how to utilize MnO_2 to load a sufficient amount of ICG in order to increase the drug loading capacity and extend the half-life of the photosensitizer, ultimately significantly improving the therapeutic efficacy of PDT.

The emerging phototherapeutic modality, PDT combined with immunotherapy, has attracted tremendous attention in the field of clinical tumor treatment attributing to their noninvasive nature, spatiotemporal controllability, and negligible cytotoxicity [32,33]. Immune checkpoint inhibitors (ICIs), primarily targeting the programmed

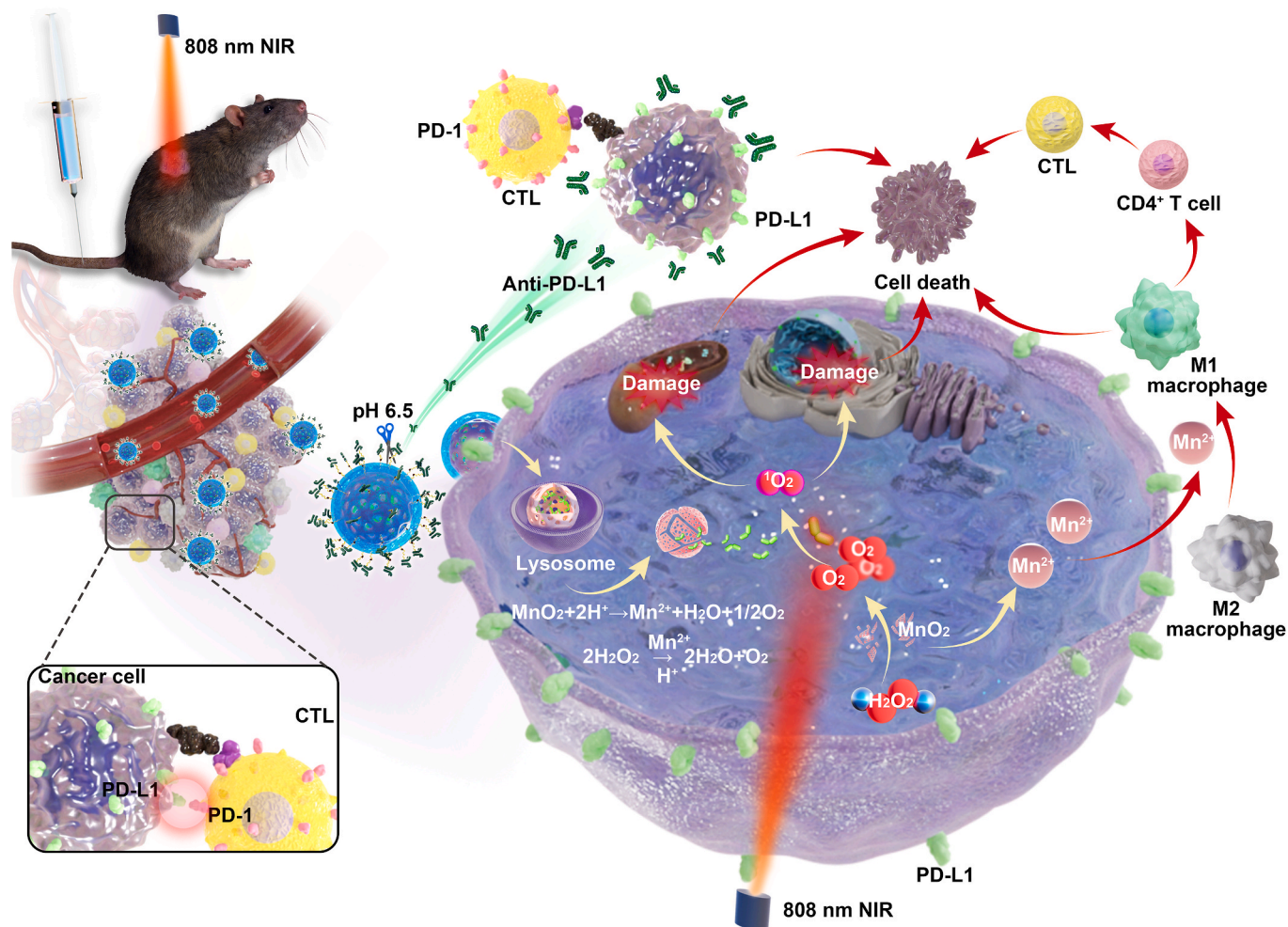
cell death receptor 1 (PD-1) and its ligand the programmed cell death receptor ligand 1 (PD-L1), continue to be the mainstay of cancer immunotherapy [34,35]. Specifically, the binding of PD-L1 on the surface of tumor cells with PD-1 on the surface of T lymphocytes inhibits T cell activity, allowing tumor cells to evade attack by T lymphocytes [36]. The advent of ICIs, particularly PD-1/PD-L1, has reshaped the treatment landscape of NSCLC: PD-L1 antibodies can block the PD-1/PD-L1 signaling pathway, restoring the function of T cells to restrain NSCLC tumor cells [37]. Whereas, the overall response rate to PD-1/PD-L1 blockade therapy in NSCLC patients remains low, less than 20 %, and many responders also develop resistance [38,39]. And the limited effectiveness can be attributed to the presence of immunosuppressive cells in the hypoxic TME, leading to immunosuppression of the tumor [40,41]. Therefore, overcoming immune escape and activating the body's immune function to eliminate tumors is the main focus of current immunotherapy research. Dendritic cells (DCs) are the most potent antigen-presenting cells (APCs) discovered to date [42]. Exosomes, as a natural nanoscale vesicle, are often used as carriers for drug delivery [43], and exosomes derived from DCs carry a large number of characteristic proteins from their parent cells, especially MHC molecules that are associated with immune activation [44]. Due to these characteristics, DCs-derived exosomes could play a momentous role in tumor immunotherapy. Inspired by these advances, our objective is to develop a synergistic treatment approach for NSCLC by combining PDT with immunotherapy and utilizing the delivery capabilities of DCs-derived exosomes, to address the challenges posed by the hypoxic and immunosuppressive TME, enhance the effectiveness of PDT and immunotherapy, and achieve precision therapy.

Herein, we have constructed hollow MnO_2 NPs loaded with ICG ($ICG@MnO_2$), and then are encapsulated in DCs-derived exosomes treated with azide-choline (AECho) via click chemistry reaction to obtain $ICG@MnO_2@Exo$. Subsequently, the exosomes are reprogrammed using PD-L1 monoclonal antibodies (anti-PD-L1), generating $ICG@MnO_2@Exo$ -anti-PD-L1 to effectively modulate the TME and combat NSCLC through the synergistic effects of PDT and immunotherapy (Scheme 1). $ICG@MnO_2@Exo$ -anti-PD-L1 is injected through the tail vein. By specifically targeting cancer cells with high PD-L1 expression, the $ICG@MnO_2@Exo$ -anti-PD-L1 NPs are precisely delivered to the tumor sites and controlled release anti-PD-L1 in the acidic TME, thereby activating T cell responses. Upon internalization by cancer cells, MnO_2 catalyzes the conversion of H_2O_2 to O_2 , alleviating tumor hypoxia. In addition, ICG utilizes O_2 to generate singlet oxygen (1O_2) under near-infrared (NIR) irradiation at 808 nm, leading to the destruction of tumor cells. Furthermore, the high levels of H_2O_2 reduce MnO_2 to Mn^{2+} , which remodels the immune microenvironment by polarizing macrophages from M2 to M1, thereby further stimulating T cell responses. Summarily, the findings of this study suggest that $ICG@MnO_2@Exo$ -anti-PD-L1 NPs can serve as a novel drug delivery platform for achieving multimodal therapy for NSCLC by combining synergy of PDT and immunotherapy modalities, which possesses less invasiveness, good clinical efficiency, and low side effects. Our goal is to provide an innovative platform for NSCLC, aiming to improve the effectiveness of PDT and immunotherapy by comprehensively improving the tumor immune microenvironment. We anticipate that with ongoing advancements in ultra-miniature fiber optic endoscopy, PDT can be effectively utilized for the treatment of deep-seated lung tumors. This progress holds the potential to broaden the scope of clinical translation and application in the future.

2. Results

2.1. Preparation and characterization of $ICG@MnO_2@Exo$ -anti-PD-L1 NPs

The synthesis process of $ICG@MnO_2@Exo$ -anti-PD-L1 NPs was visually presented in Fig. 1A. Initially, SiO_2 NPs were synthesized using

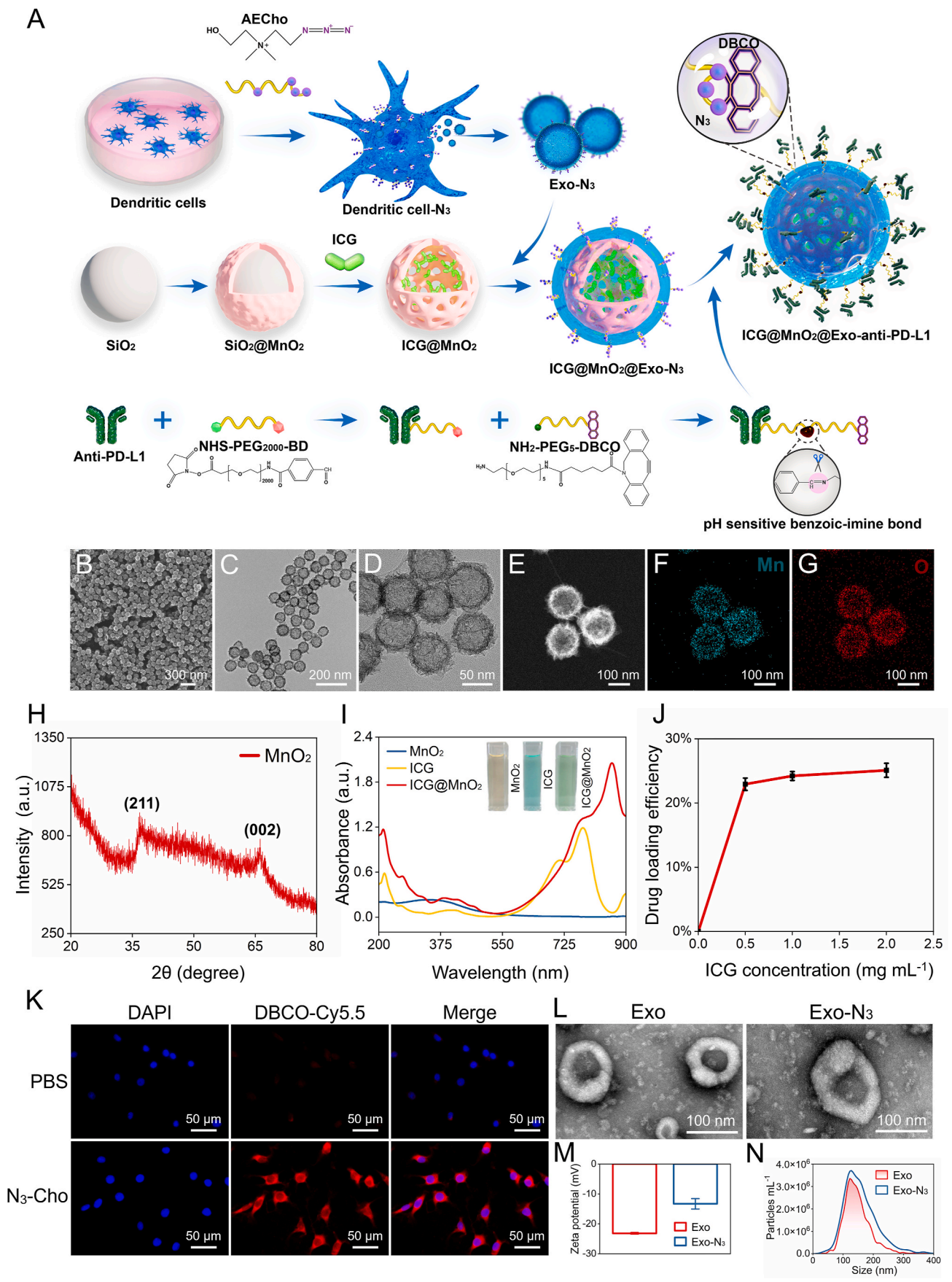


Scheme 1. Schematic illustration of reprogramming exosomes for immunity-remodeled photodynamic therapy against non-small cell lung cancer (NSCLC) *in vivo*. Firstly, an LLC (Lewis lung carcinoma cells) allograft model in C57BL/6 mice was constructed and ICG@MnO₂@Exo-anti-PD-L1 was injected through the tail vein. By specifically targeting cancer cells with high PD-L1 expression, the ICG@MnO₂@Exo-anti-PD-L1 nanospheres (NPs) are precisely delivered to the tumor site and release anti-PD-L1 in the acidic TME, thereby activating T cell responses. Upon internalization by cancer cells, MnO₂ catalyzes the conversion of hydrogen peroxide (H₂O₂) to oxygen, alleviating tumor hypoxia. In addition, ICG utilizes oxygen to generate singlet oxygen (¹O₂) under near-infrared (NIR) irradiation at 808 nm, leading to the destruction of tumor cells. Furthermore, the high levels of intratumoral H₂O₂ reduces MnO₂ to Mn²⁺, which remodels the immune microenvironment by polarizing macrophages from M2 to M1, thereby further stimulating T cell responses. Collectively, the findings of this study suggest that ICG@MnO₂@Exo-anti-PD-L1 NPs can serve as a novel drug delivery platform for achieving multimodal therapy for NSCLC by combining PDT with immunotherapy.

established methods as described in the literature [29]. Subsequently, potassium permanganate (KMnO₄) was introduced into SiO₂ NPs solution under ultrasonic conditions, leading to the formation of a MnO₂ nanoshell uniformly coating SiO₂ NPs, referred to as SiO₂@MnO₂ NPs. These were further processed by dispersing in saturated sodium carbonate (Na₂CO₃) solution and heating overnight (60 °C, 700 rpm) to etch away the SiO₂ component, ultimately yielding hollow MnO₂ NPs. The morphology and size distribution of the hollow MnO₂ NPs was confirmed by scanning electron microscopy (SEM) and transmission electron microscopy (TEM), revealing a distinct hollow structure and highly uniform size distribution of approximately 100 nm, as shown in Fig. 1B–D. Further analysis utilizing scanning TEM (STEM) coupled with energy dispersive X-ray spectroscopy (EDX) and Energy-dispersive spectroscopy (EDS) demonstrated the presence of manganese (Mn) and oxygen (O) in the MnO₂ NPs, as depicted in Fig. 1E–G and Fig. S1A. The MnO₂ NPs were also confirmed through X-ray diffraction (XRD) and Raman spectroscopy. Specifically, the XRD results displayed characteristic peaks of MnO₂ at 35.6° and 65.7° as shown in Fig. 1H, corresponding to the (211) and (002) crystal planes of birnessite-type MnO₂ (δ-MnO₂) [45], while the Raman spectra exhibited peaks at 648 cm⁻¹, 570 cm⁻¹, and 501 cm⁻¹ corresponding to δ-MnO₂ (Fig. S1B) [46].

These findings collectively validated the successful synthesis of hollow MnO₂ NPs. Mesoporous shells, with their hollow nanostructure, have been proven to be excellent drug delivery systems capable of accommodating a large number of therapeutic drugs, and the release of these drugs can be precisely controlled by adjusting the shell structure or coatings [47,48]. The hollow MnO₂ nanoplatform not only provides tumor microenvironment-specific imaging and drug release capabilities but also alleviates hypoxic conditions, thereby stimulating the body's anti-tumor immune response [20]. Therefore, in this study, hollow MnO₂ was utilized as the basis of drug delivery system.

Afterward, we incorporated ICG, a photosensitizer, into the previously synthesized hollow MnO₂ NPs to facilitate photodynamic therapy. Firstly, the photodynamic therapy efficacy of ICG was assessed by ¹O₂ generation under 808 nm laser irradiation with a singlet oxygen probe called 9,10-Anthracenediyl-bis(methylene) dimaleonic acid (ABDA). As demonstrated in Fig. S1, C and D, UV-Vis spectra recorded the ¹O₂ production of ABDA as well as the consumption of ICG. It was also noted that while ICG underwent hydrolysis in an aqueous solution, it showed enhanced stability in a DMSO solution (Fig. S1, E and F). Therefore, DMSO was employed as the solvent to minimize ICG loss during the loading process to MnO₂ NPs. Upon loading ICG into the MnO₂ NPs, a



(caption on next page)

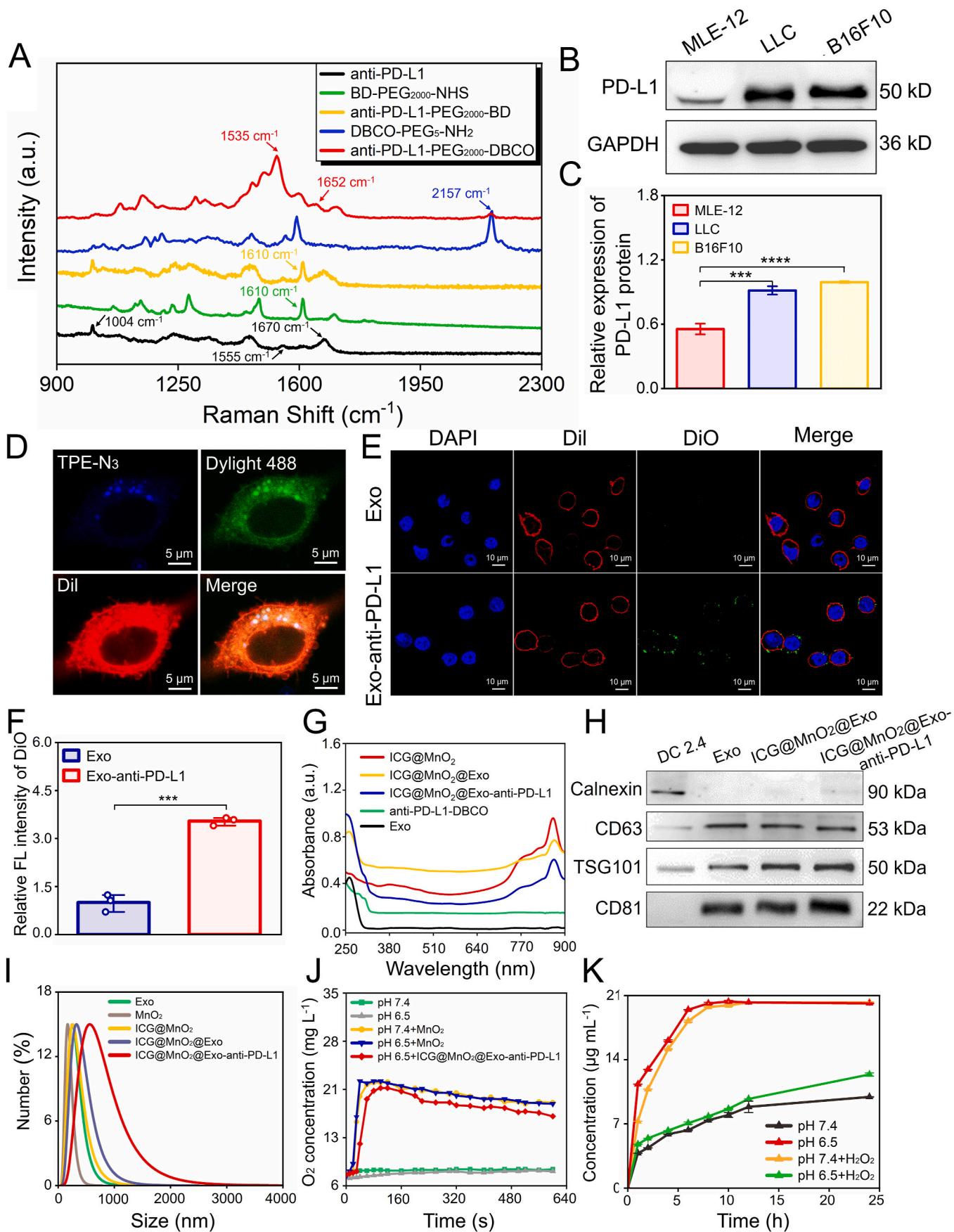
Fig. 1. Preparation and characterization of ICG@MnO₂ NPs and exosomes. (A) Schematic illustration of the synthesis process of the ICG@MnO₂@Exo-anti-PD-L1 NPs. (B, C and D) Scanning electron microscopy (SEM) and transmission electron microscopy (TEM) images of MnO₂ NPs with uniform size and morphology. (E, F and G) Energy dispersive X-ray spectroscopy (EDX) analysis of Mn and O, respectively, on the MnO₂ NPs. (H) X-ray diffraction (XRD) of MnO₂ NPs. (I) UV–Vis absorption spectra of MnO₂, free ICG and ICG@MnO₂ NPs. (J) The curve of ICG loading efficiency to MnO₂ NPs with different feeding concentrations of ICG. (K) Representative fluorescent images of dendritic cells (DC) stained with DBCO-Cy5.5 after treatment with AECho and the nuclei stained with 4',6-diamidino-2-phenylindole (DAPI) (red: DBCO-Cy5.5, blue: nuclei). Scale bar: 50 μm. (L) TEM images of Exo and Exo-N₃. Scale bar: 100 nm. (M) Zeta potential of Exo and Exo-N₃ (n = 3). (N) Nanoparticle Tracking Analysis (NTA) of Exo and Exo-N₃.

prominent change in the color of the MnO₂ solution was observed. Subsequently, the UV–Vis absorption spectra of different NPs were captured. In contrast to ICG, which exhibited an absorption peak at 780 nm, the UV–Vis absorption peaks of ICG in ICG@MnO₂ (890 nm) displayed a noticeable red shift (Fig. 1I). This shift in absorption wavelength could be attributed to the J-aggregation of ICG within the MnO₂ NPs [49]. Then EDX analysis identified the presence of carbon (C), Mn and O distribution both inside the MnO₂ NPs and on the surface, signifying that ICG was successfully loaded to MnO₂ NPs (Fig. S1, G to K). The loading efficiency of ICG in ICG@MnO₂ was calculated as 24.5 % using the formula: (Entrapped ICG in MnO₂/Total ICG@MnO₂) × 100 % (Fig. 1J and Fig. S1L).

Following this, to ensure the stability and safety of ICG@MnO₂ NPs, we employed exosomes for encapsulation. Functionalized exosomes can be modified to enhance their targeting [50]. Here, we utilized DCs treated with AECho to obtain DC-derived exosomes. AECho serves as a substrate for cells to synthesize phosphatidylcholine, a crucial component of cell membranes [51,52]. This modification introduced azide (N₃) groups to the cells, leading to the acquisition of N₃-modified exosomes (Exo-N₃). The optimal concentration of AECho for culturing the DCs in this study was determined to be 16 μg mL⁻¹ through a cell counting kit-8 (CCK8) assay (Fig. S2A). To verify the incorporation of N₃ groups into the DC membrane, DBCO-Cy5.5 was employed as a probe that undergoes click chemistry with N₃ to detect the presence of azide on the DC membrane. Confocal laser scanning microscopy (CLSM) results demonstrated the existence of positive fluorescent signals from Cy5.5 on AECho-treated cells, indicating the successful incorporation of N₃ groups into the cell membrane (Fig. 1K). Subsequently, exosomes were isolated from the supernatant of the cell culture using differential centrifugation. TEM analysis revealed the characteristic saucer-shaped morphology of the isolated exosomes (Fig. 1L). Subsequently, the Zeta potential (ζ) of exosomes derived from N₃-modified DCs exhibited a notable increase compared to regular exosomes, indicating the successful incorporation of N₃ (Fig. 1M). Furthermore, the findings from nanoparticle tracking analysis (NTA) suggested that the N₃ modification did not cause a significant change in the particle size of the Exos (Fig. 1N). Here, we supplemented the identification of N₃ on exosomes using Raman spectroscopy. As shown in Fig. S2B, the Raman spectra exhibited peaks at 1004 cm⁻¹ corresponding to characteristic peaks of proteins on Exos, peaks at 1295 cm⁻¹, 1440 cm⁻¹ corresponding to CH₂-twisting mode and CH₂-bending mode of phospholipid, while peaks at 1938 cm⁻¹, 1980 cm⁻¹, 2030 cm⁻¹ corresponding to N₃ group, illustrating that, after co-incubation with azide-choline, the exosomes secreted by DC cells do carry the N₃ group on their membrane surfaces. For clarification, all subsequent mentions of exosomes in this paper refer to EXO-N₃. After that, the Exos and ICG@MnO₂ NPs underwent multiple extrusions using a liposome extruder for 20 cycles, resulting in the formation of relatively homogeneous ICG@MnO₂@Exo NPs.

Thereafter, Exos were reprogrammed with anti-PD-L1 to obtain ICG@MnO₂@Exo-anti-PD-L1. Specifically, firstly, the benzaldehyde-PEG₂₀₀₀-NHS linker (BD-PEG₂₀₀₀-NHS) was reacted with the amino-terminal of anti-PD-L1 to form anti-PD-L1-PEG₂₀₀₀-BD. Then, anti-PD-L1-PEG₂₀₀₀-BD was linked to DBCO-PEG₅-NH₂, forming an acid-sensitive benzoic-imine bond and resulting in the synthesis of anti-PD-L1-PEG₂₀₀₀-DBCO, which allowed controlled release of anti-PD-L1 in the acidic TME with pH 6.5 [53]. Raman spectroscopy (Fig. 2A) confirmed the successful synthesis of anti-PD-L1-PEG₂₀₀₀-DBCO by identifying characteristic peaks corresponding to the PD-L1 antibody (peaks at

1004 cm⁻¹, 1555 cm⁻¹ and 1670 cm⁻¹) [54], aromatic C–C on-ring stretch (peak at 1610 cm⁻¹) [55], alkynyl group (peak at 2157 cm⁻¹) [56], and benzoic-imine bond (peak at 1535 cm⁻¹: C=C stretching, 1652 cm⁻¹: C=NH⁺ vibration) [57,58]. To validate the targeting ability of anti-PD-L1-PEG₂₀₀₀-DBCO in vitro, we employed Lewis Lung Carcinoma (LLC) cells as a representative cell line for NSCLC owing to high expression of PD-L1, while Mouse Lung Epithelial cells (MLE-12) and Mouse Melanoma cells (B16F10) served as negative and positive controls, respectively. As presented in Fig. 2B and C, western blot was conducted to verify the highly expressed PD-L1 in NSCLC cells. Additionally, to confirm the presence of DBCO groups in anti-PD-L1-PEG₂₀₀₀-DBCO, we conjugated TPE-N₃ with anti-PD-L1-PEG₂₀₀₀-DBCO and co-incubated it with LLC cells. CLSM imaging showed co-localization of TPE and anti-PD-L1 fluorescence in the LLC cell membranes, indicating the presence of reactive DBCO groups in anti-PD-L1-PEG₂₀₀₀-DBCO and its effective targeting ability to LLC cells (Fig. 2D). Furthermore, anti-PD-L1-PEG₂₀₀₀-DBCO were linked with DiO-labeled Exos to form Exo-anti-PD-L1 and incubated with DiI-labeled LLC cells. CLSM results revealed a significant fluorescence signal of DiO in the Exo-anti-PD-L1 group compared to the Exo-alone treatment group, implying that anti-PD-L1-PEG₂₀₀₀-DBCO successfully modified Exos and endowed Exos with the capacity of targeting LLC (Fig. 2E and F). Additionally, we conducted Fluorescence Recovery After Photobleaching (FRAP) experiments to further investigate the fusion between exosomes and the cell membrane, and the results showed that laser-induced quenching of membrane fluorescence within the red circle, and over time, due to the mobility of the cell membrane, the fluorescence in that area gradually recovers, indicating the fusion of DiO-Exo with cell membrane (Fig. S2C). Besides, the binding of anti-PD-L1-PEG₂₀₀₀-DBCO to Exos was quantified by the enzyme-linked immunosorbent assay (ELISA) (Fig. S2D), demonstrating that a maximum of 2.4 μg of anti-PD-L1-PEG₂₀₀₀-DBCO was bound to 100 μg of Exos. These results confirmed the successful modification of Exos by anti-PD-L1-PEG₂₀₀₀-DBCO. Afterward, the responsiveness of the benzoic-imine bond on Exo-anti-PD-L1 to acidic environments was validated by ELISA detection of anti-PD-L1 in the dialysate, which showed a more release of anti-PD-L1 at pH 6.5 compared to pH 7.4 (Fig. S2E). Subsequently, the anti-PD-L1-PEG₂₀₀₀-DBCO was incubated with ICG@MnO₂@Exo NPs to prepare ICG@MnO₂@Exo-anti-PD-L1 NPs. The UV–Vis absorbance spectra of ICG@MnO₂@Exo-anti-PD-L1 NPs and their intermediates were analyzed (Fig. 2G). The results showed that the absorption peaks of Exos and anti-PD-L1-PEG₂₀₀₀-DBCO appeared on the UV–Vis spectrum of the ICG@MnO₂@Exo-anti-PD-L1 NPs, indicating that ICG@MnO₂@Exo-anti-PD-L1 NPs were successfully constructed. Additionally, the western blot analysis confirmed that the markers of Exos including CD63, TSG101, and CD81 [59] were enriched in the ICG@MnO₂@Exo-anti-PD-L1 NPs, while the negative marker calnexin was not detected (Fig. 2H). Furthermore, the particle size of the NPs, as determined by dynamic light scattering (DLS), increased sequentially with the modifications (Fig. 2I). Notably, the particle size obviously increased after the ligation of anti-PD-L1-PEG₂₀₀₀-DBCO, which could be attributed to the formation of a hydrated cloud with a large excluded volume due to the hydrophilic nature of the PEG chains in the linkers [60]. Then, the ability of ICG@MnO₂@Exo-anti-PD-L1 NPs to catalyze the decomposition of H₂O₂ into O₂ across various pH levels was investigated. Similar to MnO₂, ICG@MnO₂@Exo-anti-PD-L1 NPs demonstrated O₂ production (Fig. 2J), demonstrating that they preserved the catalytic properties of MnO₂. Given that MnO₂ can react with



(caption on next page)

Fig. 2. Synthesis and characterization of ICG@MnO₂@Exo-anti-PD-L1 NPs. (A) Raman spectra of anti-PD-L1, BD-PEG₂₀₀₀-NHS, anti-PD-L1-PEG₂₀₀₀-BD, DBCO-PEG₅-NH₂ and anti-PD-L1-PEG₂₀₀₀-DBCO. (B and C) Western blot and statistical diagram of PD-L1 in LLC, with MLE-12 (mouse lung epithelial cells) and B16F10 (mouse melanoma cells) as the negative and positive control, respectively (n = 3). (D) Confocal laser scanning microscopy (CLSM) imaging of TPE-N₃ staining in LLC treated with anti-PD-L1-PEG₂₀₀₀-DBCO. Scale bar: 5 μm. (E and F) CLSM imaging and quantitative analysis of LLC co-incubated with Exo or Exo-anti-PD-L1 (n = 3). Scale bar: 10 μm. (G) UV–Vis absorption spectra of different groups. (H) Western blot analysis of exosome markers (CD63, TSG101 and CD81) and the negative marker (calnexin) in different groups. (I) Dynamic light scattering (DLS) detection of the sizes of different groups. (J) Dissolved oxygen-time curve of MnO₂ and ICG@MnO₂@Exo-anti-PD-L1 in PBS solutions containing H₂O₂ at different pH (pH 6.5 or 7.4). (K) The release curve of ICG from ICG@MnO₂@Exo-anti-PD-L1 NPs in H₂O₂ solutions at different pH levels (pH 6.5 or 7.4). ***P < 0.001, and ****P < 0.0001, respectively.

H⁺ and H₂O₂ in TME to form harmless water-soluble Mn²⁺ [61,62], the degradation of MnO₂ in H₂O₂ solutions at different pH levels in this study was evaluated by analyzing the absorbance of MnO₂ at 309 nm using UV–Vis spectroscopy (Figs. S2F and G). It is exhibited that MnO₂ could be decomposed in H₂O₂ (100 μM), with a faster degradation rate observed in acid solution. As MnO₂ degraded, the structure of ICG@MnO₂@Exo-anti-PD-L1 NPs collapsed, resulting in the release of ICG into the solution. The UV–Vis absorption of ICG at 780 nm revealed an increase in the amount of released ICG over time, with higher releasing efficiency observed in H₂O₂ (Fig. S2H and Fig. 2K). These observations suggest that ICG@MnO₂@Exo-anti-PD-L1 NPs not only effectively generate O₂ but also concurrently release ICG. Such dual functionality is beneficial in enhancing the photodynamic effect of ICG, potentially improving the efficacy of photodynamic therapy in cancer treatment.

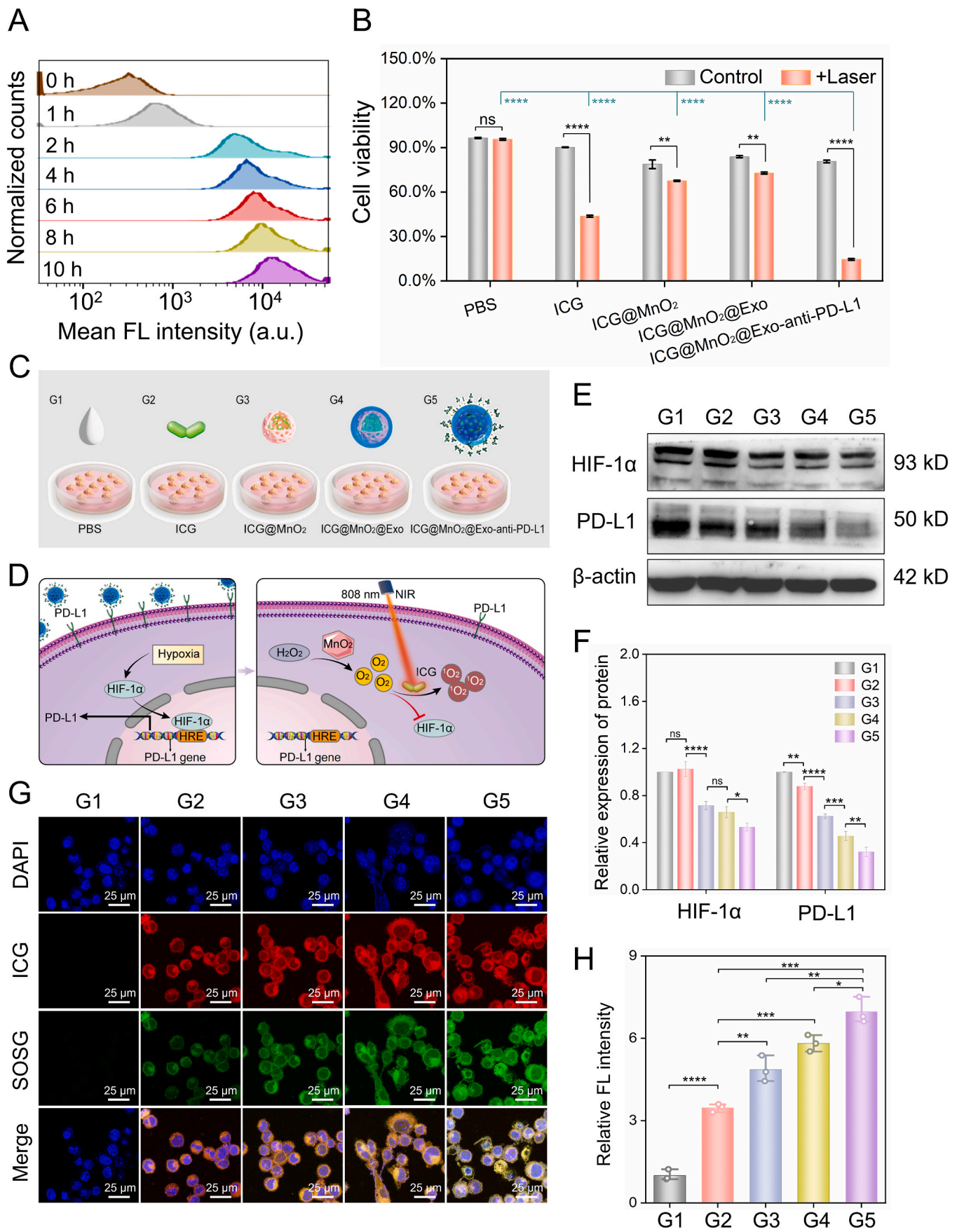
2.2. Enhanced photodynamic effects of ICG@MnO₂@Exo-anti-PD-L1 NPs in vitro

To evaluate the PDT efficacy of ICG@MnO₂@Exo-anti-PD-L1 NPs, we conducted a series of in vitro experiments using the LLC cell line. The optimal concentration of ICG in NPs for LLC culture was determined to be 2 μg mL⁻¹ by the CCK8 assay (Fig. S3A). The next step involved analyzing the uptake of these nanoparticles by LLC cells. Flow cytometry results indicated significant internalization of ICG@MnO₂@Exo-anti-PD-L1 by the cells within 2 h, with endocytosis levels increasing over prolonged incubation periods (Fig. 3A). Then, cytotoxicity of ICG@MnO₂@Exo-anti-PD-L1 NPs on cells was evaluated by the CCK-8 assay and the results showed that ICG@MnO₂@Exo-anti-PD-L1 NPs under 808 nm NIR irradiation exhibited a more pronounced cytotoxic effect on tumor cells compared to other groups (Fig. 3B). This enhanced effect may be attributed to the targeting effect of anti-PD-L1, which led to the accumulation of more NPs in the cells, thereby augmenting the cytotoxic effects. However, the therapeutic efficacy of PDT is significantly impeded by the hypoxic microenvironment prevalent in tumors, as PDT relies on the presence of oxygen. Therefore, it becomes crucial to mitigate hypoxia within TME in order to enhance the effectiveness of PDT. It was confirmed that NPs had a strong ability to generate O₂ to effectively alleviate tumor hypoxia. In the subsequent experiments, the subjects were divided into 5 groups (G1: PBS, G2: ICG, G3: ICG@MnO₂, G4: ICG@MnO₂@Exo, G5: ICG@MnO₂@Exo-anti-PD-L1) (Fig. 3C). Western blot results showed that the expression of hypoxia-inducible factor 1α (HIF-1α), which reflected the degree of cellular hypoxia [63,64], was significantly decreased in LLC cells under hypoxic conditions in the MnO₂-treated group, particularly the G5 group. Meanwhile, the expression of PD-L1 protein was down-regulated as well in LLC cells, possibly attributing to the fact that HIF-1α is an important regulator of PD-L1 in hypoxic TME, and a decrease in HIF-1α directly leads to a subsequent reduction in PD-L1 (Fig. 3D–F) [65]. Moreover, employing pimonidazole as a hypoxia probe to evaluate LLC cells treated under hypoxic conditions with various nanoparticles, we observed a decrease in pimonidazole fluorescence correlating with increased O₂ levels. Notably, this reduction was most pronounced in the G5 group, indicating the greatest enhancement in oxygen concentration in this group (Fig. S3, B and C). The above data confirmed that ICG@MnO₂@Exo-anti-PD-L1 NPs could replenish O₂ by triggering the decomposition of H₂O₂ to effectively alleviate tumor hypoxia. Next, to assess the

enhancing effect of ICG@MnO₂@Exo-anti-PD-L1 NPs on PDT, we used the singlet oxygen sensor green (SOSG) to measure ¹O₂ production, and the fluorescence intensity in the G5 group was the strongest (Fig. 3G and H). Collectively, these results underscored that ICG@MnO₂@Exo-anti-PD-L1 NPs could significantly bolster the PDT effect in the TME by alleviating hypoxia.

2.3. Macrophage polarization induced by ICG@MnO₂@Exo-anti-PD-L1 to kill LLC in vitro

Besides catalyzing O₂ generation from H₂O₂, MnO₂ is also reduced to Mn²⁺, which could induce a phenotypic transition of tumor associated macrophages in TME from M2 to M1, leading to the remodeling of the immune microenvironment and the activation of T cells [66]. In this study, the RAW264.7 macrophage cell line was utilized to assess the polarization of macrophages upon treatment with different NPs. And we induced macrophages with IL-4 (100 ng/mL) in vitro for 24 h to polarize them into M2, and then conducted subsequent experimental studies. Firstly, flow cytometry analysis of the expression of M1 macrophage markers (CD80⁺ and CD86⁺) further supported that a higher proportion of M1 macrophages in the groups treated with NPs including in the G3 (26.7%), G4 (55.6%), and G5 (75.1%) groups, compared to G1 and G2 groups (G1: 3.46%, G2: 3.61%) (Fig. 4A). Subsequently, immunofluorescence (IF) of M1 macrophages (CD80) and total macrophages (CD11b) was assessed that in contrast to the G1 and G2 groups, the fluorescence intensity of CD80 in other groups was obviously increased (Fig. S4 A and B). Subsequent western blot analysis focusing on macrophage polarization markers, specifically the M1 marker (iNOS) and the M2 marker (Arg-1), demonstrated a decline in Arg-1 expression and an increase in iNOS expression in groups treated with MnO₂-containing nanoparticles (Fig. 4B and C). This finding aligns with existing research [67], our above results also demonstrated that NPs could increase M1 proportion due to generation of Mn²⁺. Besides, evidence has proved that Mn²⁺ activates the STING signaling pathway in macrophages, leading to the activation of the downstream NF-κB p65 signaling pathway, which induces macrophage polarization to M1 and the secretion of pro-inflammatory cytokines [68]. Herein, we also detected the effect of NPs on NF-κB p65 that NPs containing MnO₂, especially ICG@MnO₂@Exo-anti-PD-L1, could effectively augment the expression of NF-κB p65, manifesting NPs induced the polarization of macrophages from M2 to M1 probably through the NF-κB p65 pathway. Next, to evaluate the impact of RAW264.7 cells treated with different NPs on LLC cells, a co-culture system of RAW264.7 cells and LLC cells was established. The co-culture medium was collected for subsequent ELISA analysis of IL-10 and TNF-α, which were anti-inflammatory secreted by M2 and pro-inflammatory cytokines secreted by M1, respectively [69]. The outcomes revealed a reduction in IL-10 secretion and an elevation in TNF-α expression in the groups that received nanoparticle treatment (Fig. 4D–F). Additionally, ELISA analysis of high mobility group box 1 (HMGB-1), an indicator of tumor immunogenic cell death (ICD), revealed abundant HMGB-1 in the groups treated with NPs, indicating that NPs induced macrophages to secrete pro-inflammatory cytokines, leading to the ICD of tumor cells (Fig. 4G). Furthermore, the phagocytic effect of RAW264.7 cells on LLC cells was evaluated in the co-culture condition. Immunofluorescence staining for RAW264.7 (CD11b-PE, red) and LLC cells (CFSE, green) was visualized by CLSM that a marked reduction in LLC cells in the groups treated with



(caption on next page)

Fig. 3. ICG@MnO₂@Exo-anti-PD-L1 NPs alleviate cell hypoxia and enhance PDT efficiency in vitro. (A) The mean fluorescence intensity of ICG via flow cytometry analysis on uptake of ICG@MnO₂@Exo-anti-PD-L1 NPs by LLC at 0, 1, 2, 4, 6, 8, 10 h, respectively. (B) CCK-8 assay evaluated the effect of 808 nm laser on LLC cell viability after different treatment. (C) Schematic diagram of the group design: treated with G1 (PBS), G2 (ICG), G3 (ICG@MnO₂), G4 (ICG@MnO₂@Exo), G5 (ICG@MnO₂@Exo-anti-PD-L1). (D) Schematic diagram of the mechanism of MnO₂-mediated alleviation hypoxia and down-regulation of PD-L1 expression while enhancing the effect of PDT in LLC cells. (E and F) Western blot and statistical diagram of HIF-1 α and PD-L1 in LLC with different treatments. (G and H) CLSM images and quantitative analysis of ¹O₂ production in LLC with different treatments under 808 nm laser irradiation by SOSG. Scale bar: 25 μ m **P* < 0.05, ***P* < 0.01, ****P* < 0.001, *****P* < 0.0001, and ns: no significance.

NPs, with most of the tumor cells being engulfed and digested by macrophages (Fig. 4H). These observations indicated that the NPs could stimulate macrophage polarization, leading to actively engulfing tumor cells.

2.4. Targeting ability and anti-tumor effect of ICG@MnO₂@Exo-anti-PD-L1 against NSCLC in vivo

To further explore the outcomes of ICG@MnO₂@Exo-anti-PD-L1 NPs in vivo, an LLC cell allograft model in C57BL/6 mice was constructed. ICG or ICG@MnO₂@Exo-anti-PD-L1 was injected through the tail vein, and the distribution of NPs in vivo at different time points was analyzed by in vivo imaging system (IVIS). As shown in Fig. 5A and C, compared to free ICG, ICG@MnO₂@Exo-anti-PD-L1 NPs exhibited remarkable accumulation at the tumor sites with the highest fluorescence intensity after 4 h, indicating NPs possessed the effective targeting ability. Meanwhile, the circulation time of ICG@MnO₂@Exo-anti-PD-L1 NPs was prolonged in the body, suggesting an extended half-life of ICG in these NPs. Whereafter, mice were sacrificed 24 h after injection, and fluorescence quantitative analysis also showed that in contrast to major organs including heart, liver, spleen, lung as well as kidney, more ICG@MnO₂@Exo-anti-PD-L1 NPs were precisely delivered to the tumor (Fig. 5B and D). Besides, quantitative analysis of fluorescence intensity exhibited that the fluorescence intensity in the spleen and kidney was higher in the ICG@MnO₂@Exo-anti-PD-L1 group compared to the ICG group (Fig. 5D). This phenomenon is attributed to the abundant presence of immune cells expressing PD-L1 in the spleen [65], which leads to the accumulation of NP in this organ. Additionally, the kidneys are responsible for clearing NPs from the bloodstream, resulting in high signals in the kidney region [70]. Interestingly, the fluorescence intensity in the liver was lower in the ICG@MnO₂@Exo-anti-PD-L1 group than ICG group (Fig. 5D). This can be ascribed to the fact that ICG is typically metabolized by the liver, but when ICG is encapsulated within NPs, serum proteins are unable to combine with ICG, thereby hardly entering the liver [71].

After that, to investigate the anti-tumor therapeutic effect of our ICG@MnO₂@Exo-anti-PD-L1 NPs, mice were administrated with different treatments when the tumor volume reached 100 mm³, followed by 808 nm laser irradiation on day 0, 4, and 8 (Fig. 5E). On the 9th day of treatment, blood samples were collected from mice for hematological and biochemical analyses. The results revealed that there were no significant effects on the biochemical and hematological parameters in mouse blood after the third administration, indicating the high biocompatibility of the nanomaterial (Fig. 5S). The mouse body weights and tumor volumes were monitored every 2 days, and their survival times were recorded. As shown in Fig. 5F, the body weights of all mice remained relatively stable throughout the experiment, indicating the high biosafety of ICG@MnO₂@Exo-anti-PD-L1 NPs. Additionally, the tumor growth curves (Fig. S6A) and the relative changes in tumor volume (V/V_0) during treatment were analyzed (Fig. 5G), where V_0 represents the initial tumor volume. Statistical analysis revealed that the therapeutic effect of the G3+L group was significantly superior to that of the G2+L group, indicating that MnO₂ enhanced the efficacy of PDT. Importantly, the G5+L group exhibited significantly better therapeutic outcomes than the G3+L and G4+L groups, with a 100 % survival rate observed after 36 days (Fig. 5H), suggesting that the combined treatment of PDT and immunotherapy was more effective than PDT alone. Then, tumor samples were collected on day 16 to evaluate the

therapeutic efficacy. The results demonstrated noticeable tumor reduction or even complete elimination in the G5+L group (Fig. 5I). Furthermore, the proliferation and apoptosis of tumor cells were evaluated using Ki-67 and TdT-mediated dUTP nick end labeling (TUNEL) staining [72]. It was observed that the index of Ki-67 was prominently decreased, and the fluorescence intensity of TUNEL was significantly increased in the G5+L group (Fig. 5J and Fig. S6B), implying that NPs effectively suppressed tumor cell proliferation and induced significant tumor cell apoptosis. In addition, to evaluate the impact of NPs on metastatic tumors, we performed pathological dissection on the mice, and grossly visible gray-white lesions in the lung tissue were observed in all groups except the G5+L group. Simultaneously, histological examination of the lungs confirmed the presence of metastatic tumors, indicating the occurrence of lung metastasis (Fig. 5K and Fig. S6C). The favorable outcome in the G5+L group suggested that ICG@MnO₂@Exo-anti-PD-L1 NPs not only exhibited therapeutic effects on primary tumors but also possessed the capacity to inhibit the formation of metastatic lesions. Furthermore, we evaluated the biosafety of the NPs by examining the major organs of the mice by hematoxylin and eosin (H&E) staining [73]. The results indicated that no obvious morphological changes were observed in the major organs of the mice in all groups, demonstrating the good biocompatibility of ICG@MnO₂@Exo-anti-PD-L1 NPs in mice (Fig. S7). Taken together, ICG@MnO₂@Exo-anti-PD-L1 NPs demonstrated strong targeting specificity, excellent biocompatibility, and effective inhibition of tumor growth and metastasis.

2.5. Immunity-remodeled photodynamic therapy of ICG@MnO₂@Exo-anti-PD-L1 against NSCLC

After validating the targeting ability and anti-tumor effect of ICG@MnO₂@Exo-anti-PD-L1 in animal experiments, we proceeded to identify the PDT and immunotherapy efficiency of NPs in vivo. Here, we continued to use pimonidazole to assess the hypoxic conditions in the tumor with the treatment of the NPs after irradiation with an 808 nm laser. The outcomes displayed that compared with other groups, the fluorescence intensity of pimonidazole was distinctly reduced in the G5+L group, illustrating that the hypoxia of TME was effectively alleviated (Fig. 6A and Fig. S8A). Nevertheless, the fluorescence intensity in the G2+L group was significantly higher compared to the other groups, because the PDT effect of ICG alone resulted in the consumption of O₂ within the tissue, leading to a more severe hypoxia in the tumors [74]. Then, the generation of ¹O₂ after irradiation with an 808 nm laser was evaluated by detection of SOSG and the results showed that the fluorescence intensity of SOSG in the G5+L group was significantly higher compared to the other groups, implying that ICG@MnO₂@Exo-anti-PD-L1 NPs powerfully enhanced the efficiency of PDT (Fig. 6B and Fig. S8B). Collectively, the aforementioned findings strongly indicated that ICG@MnO₂@Exo-anti-PD-L1 NPs possessed the ability to accurately target tumor sites and effectively raise the efficiency of PDT by mitigating hypoxia within the TME. Additionally, consistent with the results from in vitro experiments, WB and CLSM findings in vivo experiments demonstrated that NPs could reduce the expression of PD-L1 and HIF-1 α (Fig. 6C–F and Fig. S8C). Research reported that HIF-1 α regulates cancer cell growth by modulating the expression of genes involved in glycolysis, angiogenesis signaling, apoptosis and stress response [63]. And increased levels of HIF-1 α induced by tumor hypoxia promote the expression of PD-L1 in cancer cells and suppress immune

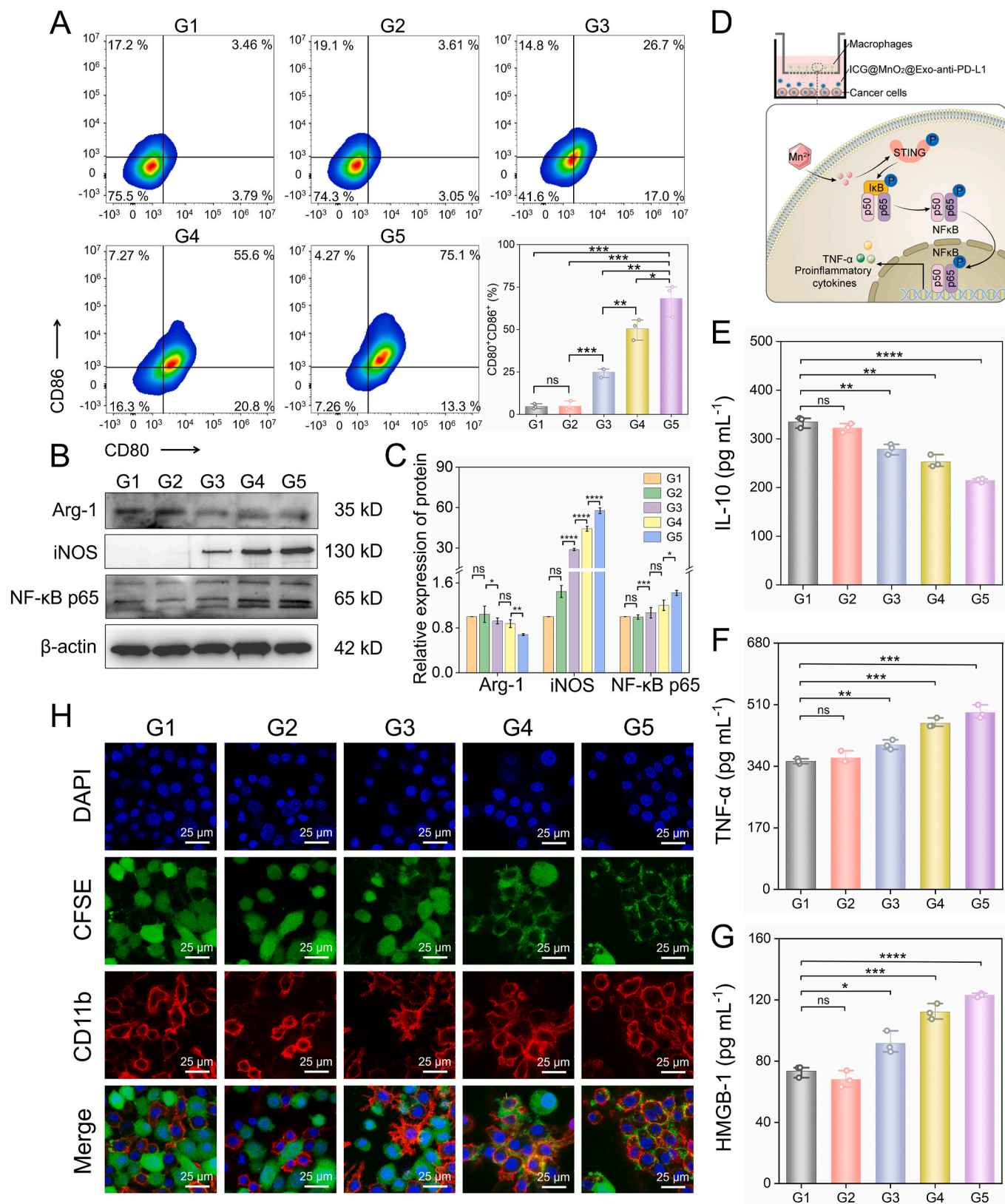


Fig. 4. Effect of ICG@MnO₂@Exo-anti-PD-L1 NPs on macrophage polarization in vitro. (A) Flow cytometry analysis on the polarization of macrophages from M2 to M1 after co-incubation with different NPs was performed by CD80 and CD86 staining. (B and C) Western blot and statistical diagram of expression of Arg-1, iNOS and NF- κ B p65 in macrophages with different treatments. (D) Schematic diagram of co-culture of LLC and M2 macrophages for cytokines detection in transwell system (E, F and G) ELISA results of the macrophage-associated cytokines (M1: TNF- α ; M2: IL-10) and tumor immunogenic cell death (ICD) marker HMGB-1. (H) CLSM images of macrophage (CD11b: red) phagocytosis of LLC (CFSE: green) in a 24-well plate with different treatments. Scale bar: 25 μ m. * P < 0.05, ** P < 0.01, *** P < 0.001, **** P < 0.0001, and ns: no significance, respectively.

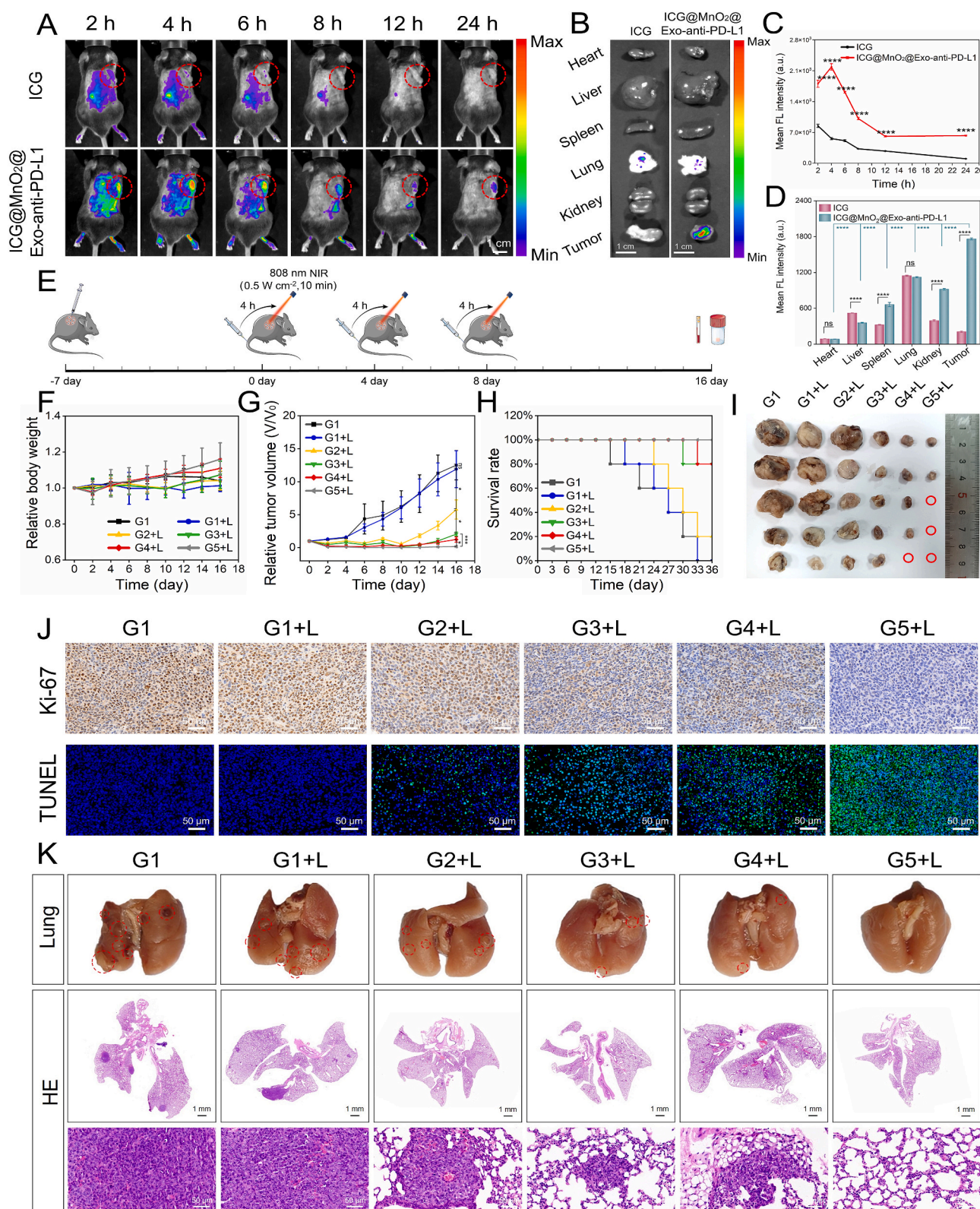
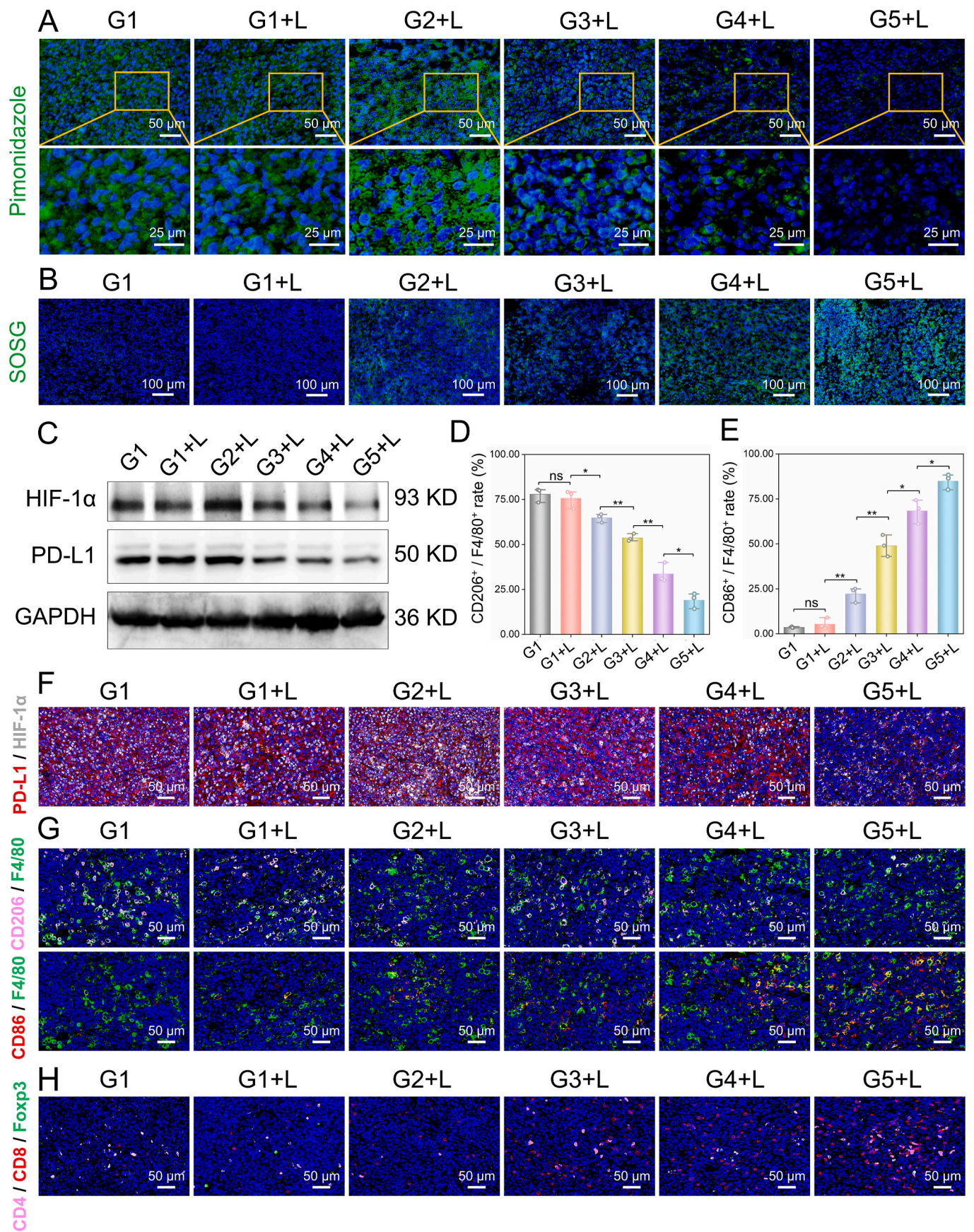


Fig. 5. In vivo targeted delivery and anti-tumor effect of ICG@MnO₂@Exo-anti-PD-L1 NPs on C57BL/6 mice bearing LLC tumor allograft. (A and C) The distribution and fluorescence quantitative intensity of free ICG and ICG@MnO₂@Exo-anti-PD-L1 NPs in mice over time (red cycles indicate the location of the tumors). Scale bar: 1 cm. (B and D) The distribution and fluorescence quantitative intensity of free ICG and ICG@MnO₂@Exo-anti-PD-L1 NPs in the main organs and tumors 24 h after injection. Scale bar: 1 cm. (E) Schematic illustration of LLC tumor allograft and treatments. (F) The body weight curves, (G) The relative tumor volume changes and (H) Survival curves of C57BL/6 mice bearing LLC tumor allograft in different groups (n = 5). (I) Digital images of tumor tissues on day 16. (J) Ki-67 and TUNEL staining of tumor tissues from mice in groups. Scale bar: 50 μm. (K) Gross observations of lung tissues (red arrows represent metastasis) and representative H&E staining images of the metastases in lung tissues. *P < 0.05, ***P < 0.001, ****P < 0.0001, and ns: no significance, respectively.



(caption on next page)

Fig. 6. In vivo evaluation of PDT and immunity efficiency of ICG@MnO₂@Exo-anti-PD-L1 NPs. (A) CLSM images and quantitative analysis of pimonidazole to detect the effect of NPs on alleviating hypoxia in different groups. Scale bar: 100 μm. (B) CLSM images and quantitative analysis of singlet oxygen sensor green (SOSG) to evaluate ¹O₂ content in mouse tumor tissues in different groups. Scale bar: 100 μm. (C) Western blot of HIF-1α and PD-L1 in mouse tumor tissues with different treatments (n = 3). (D, E and F) CLSM images of HIF-1α and PD-L1 in tumor tissues of mice with different treatment groups (white: HIF-1α, red: PD-L1). Scale bar: 50 μm. (D, E and G) CLSM images and quantitative analysis of the CD206 or CD86-positive macrophages over total macrophages (F4/80) in mouse tumor tissues with different groups (green: F4/80 marked total macrophages, pink: CD206 marked M2 macrophages, red: CD86 marked M1 macrophages). Scale bar: 50 μm. (H) T cell infiltration in tumor tissues of mice with different treatment groups (green: Foxp3, red: CD8, pink: CD4). Scale bar: 50 μm. *P < 0.05, **P < 0.01, and ns: no significance, respectively.

responses [65]. Therefore, ICG@MnO₂@Exo-anti-PD-L1 NPs inhibited the expression of HIF-1α by alleviating hypoxia, leading to a further reduction in PD-L1 levels within tumor cells. The downregulation of PD-L1 in tumor cells, together with the anti-PD-L1 of the NPs, synergistically activate T cells. Thereafter, considering the roles of MnO₂ and anti-PD-L1 in tumor immune remodeling, we performed immunofluorescence staining of immune-related molecules in the tumor tissue. The results revealed that the G5+L group exhibited a higher proportion of CD86⁺ (M1 marker) cells among total macrophages (F4/80⁺) compared to other treatment groups, along with a decrease in the proportion of CD206⁺ (M2 marker) cells (Fig. 6D, E, G), indicating that ICG@MnO₂@Exo-anti-PD-L1 NPs induced macrophage polarization towards the M1 phenotype in vivo. Besides, a tumor-infiltrating T cell is one of the most important effector cells in the immune response to cancer [75], and high levels of T cell infiltration are often associated with a favorable anti-tumor immune response and prognosis [76]. T cell infiltration can induce tumor cell apoptosis, inhibit tumor growth and spread, and enhance the patient's sensitivity to treatment [77]. Therefore, evaluating T cell infiltration can provide important information for tumor treatment and prognosis assessment. In our immunofluorescence results, we observed an increased presence of CD8⁺ T cells and CD4⁺ T cells, accompanied by a noticeable decrease in the proportion of Treg cells (Foxp3⁺) cells in the NPs treatment group (Fig. 6H), suggesting that ICG@MnO₂@Exo-anti-PD-L1 NPs effectively reshaped the tumor immune microenvironment and promoted immune rejuvenation. In summary, our findings suggested that ICG@MnO₂@Exo-anti-PD-L1 NPs demonstrated remarkable PDT and immunotherapy effects to effectively inhibit tumor progression, suppress lung metastasis, and reshape the tumor immune microenvironment in mice.

3. Discussion

The prognosis for advanced NSCLC remains unsatisfactory, largely due to high morbidity and mortality [4,78]. Consequently, there is a pressing need for alternative approaches that offer reduced invasiveness, enhanced clinical efficacy, and minimal adverse effects. The combination of PDT and immunotherapy has risen sharply to a promising approach for high-grade malignant NSCLC. Nevertheless, owing to the absence of precise drug delivery techniques and the hypoxic and immunosuppressive characteristics of the TME, the efficacy of this combination therapy approach is less than ideal. In this study, we successfully developed an innovative nanodelivery system termed ICG@MnO₂@Exo-anti-PD-L1 NPs using engineered exosomes with high targeting ability, prolonged circulation time, and excellent biocompatibility to integrate PDT with immunotherapy for NSCLC. The platform consisted of hollow MnO₂ NPs loaded with the ICG (ICG@MnO₂), encapsulated within exosomes that were reprogrammed with anti-PD-L1 to eventually form ICG@MnO₂@Exo-anti-PD-L1. This system demonstrated several therapeutic effects. Firstly, it enabled specific delivery of the ICG@MnO₂@Exo-anti-PD-L1 NPs to the tumor sites by targeting high PD-L1 expression of cancer cells. Once within the acidic TME, the NPs released anti-PD-L1 to activate T cell responses. Furthermore, when taken up by cancer cells, MnO₂ catalyzed the conversion of H₂O₂ to O₂, thereby mitigating tumor hypoxia. Simultaneously, ICG utilized the O₂ to generate ¹O₂ under 808 nm NIR irradiation, inducing tumor cell death for PDT. Moreover, the high levels of intratumoral H₂O₂ reduced MnO₂ to Mn²⁺, reshaping the immune microenvironment by polarizing

macrophages from M2 to M1 and further enhancing T cell responses. In conclusion, this study demonstrated that the ICG@MnO₂@Exo-anti-PD-L1 NPs served as a promising drug delivery platform for achieving multimodal therapy in NSCLC. This approach provides a novel perspective that encourages further exploration of the combination of PDT with immunotherapy for cancer treatment.

In the realm of therapeutic modalities, PDT, which stands out as a technique that offers spatiotemporal control over the generation of ROS, is activated by focused laser light through employing a photosensitizer targeted at the afflicted site, resulting in effective tumor ablation [79]. However, it is important to note that PDT, in some cases, can lead to increased tumor hypoxia levels, which may hinder complete tumor eradication. The ICG@MnO₂@Exo-anti-PD-L1 nanodelivery system presented in this study combines hollow MnO₂ NPs loaded with the ICG (ICG@MnO₂). Mesoporous shells, characterized by their hollow nanostructure, have been established as highly effective drug loading and delivery systems, capable of accommodating a wide range of therapeutic drugs [80]. In this study, the hollow MnO₂ nanoplatform demonstrates a significant advantage by virtue of its hollow structure, which enables a more substantial drug loading. This increased drug loading capacity extends the half-life of the photosensitizer, leading to a substantial enhancement in the therapeutic effectiveness of PDT. Apart from this, the nanodelivery system could mitigate tumor hypoxia by catalyzing the conversion of H₂O₂ into O₂ through MnO₂ [23]. More importantly, the generation of Mn²⁺ by redox reaction, thereby polarizing macrophages from the M2 to M1, further enhance T cell responses [66]. Therefore, employing this material as a framework enables a higher loading capacity for photosensitizers to conduct PDT. Simultaneously, it also serves a regulatory role in the tumor immune microenvironment.

Numerous approaches have been devised to tackle the immunosuppressive microenvironment found in malignant tumors, including the use of immune checkpoint blockade antibodies directed at PD-1, PD-L1, and CTLA-4 [34,35]. In this study, to further enhance the efficiency of the immune response, we conducted multidimensional design. Firstly, we applied anti-PD-L1 to target specially PD-L1 highly expressed cancer cells to controllably release anti-PD-L1 in the acidic TME, thereby activating T cell response. Secondly, the high levels of intratumoral H₂O₂ reduce MnO₂ from our NPs to Mn²⁺, polarizing M2 macrophages to M1, thereby further stimulating T cell responses. Furthermore, NPs induced macrophages to secrete pro-inflammatory cytokines, leading to the ICD of tumor cells. In addition, due to the expression of MHC molecules, exosomes derived from DCs may be participated in immune activation. The tumor immune microenvironment is inherently complex, and we aim to enhance the effectiveness of immunotherapy from multiple angles. Unlike traditional anti-PD-1/PD-L1 monoclonal antibodies that only disrupted the receptor-ligand binding on the cell membrane surface, our novel NPs also regulated the PD-L1-mediated signaling pathways within cancer cells, enhancing the therapeutic effects. This is similar to the findings of other studies. TPP-LND is created by combining mitochondrial-targeted triphenylphosphine cations (TPP⁺) with the anticancer agent lonidamine (LND), then enclosed in liposomes to form TPP-LND@Lip nanoparticles. These nanoparticles sensitize radiotherapy (RT) by reversing the tumor's hypoxic environment, causing more DNA damage, and concurrently lower PD-L1 expression through increased adenosine 5'-monophosphate-activated protein kinase activation [81]. Additionally, inhibiting mitochondrial oxidative phosphorylation (OXPHOS) could serve as an effective method to

downregulate PD-L1, and the novel PD-L1 regulation strategy based on selectively inhibiting tumor mitochondrial OXPHOS, may offer a new avenue for sensitizing immunotherapy and photodynamic therapy [82].

Notably, it is important to emphasize the clever designs of this delivery platform. In addition to the hollow MnO₂ load-bearing more photosensitizers, another two ingenious design elements have been integrated. The first element concerns ensuring the stability and safety of ICG@MnO₂ NPs, which involved using exosomes for encapsulation. In this context, DCs treated with AECho were employed to acquire DC-derived exosomes. AECho functions as a substrate for cells, facilitating the synthesis of phosphatidylcholine, a vital component of cell membranes [51,52]. This modification introduced azide (N₃) groups to the cells, resulting in the production of N₃-modified exosomes (Exo-N₃). And to ulteriorly verify the incorporation of N₃ groups into the DC membrane, DBCO-Cy5.5 was employed as a probe that undergoes click chemistry with N₃ to detect the presence of azide on the DC membrane. The second design element involves reprogramming exosomes with anti-PD-L1 to obtain ICG@MnO₂@Exo-anti-PD-L1. Specifically, firstly, the benzaldehyde-PEG₂₀₀₀-NHS linker (BD-PEG₂₀₀₀-NHS) was reacted with the amino-terminal of anti-PD-L1 to form anti-PD-L1-PEG₂₀₀₀-BD. Subsequently, anti-PD-L1-PEG₂₀₀₀-BD was linked to DBCO-PEG₅-NH₂, creating an acid-sensitive benzoic-imine bond, resulting in the synthesis of anti-PD-L1-PEG₂₀₀₀-DBCO, which allowed controlled release of anti-PD-L1 in the acidic TME with pH 6.5 [53].

Our objective is to offer a novel platform for NSCLC to enhance the efficacy of PDT and immunotherapy by addressing the inherent complexity of the tumor immune microenvironment from various angles. We believe that as ultra-miniature fiber optic endoscopy continues to advance, PDT would be applied to treat deep lung tumors effectively, advancing the possibilities of clinical translation and application in the future. Nonetheless, concerning the feasibility of implementing our strategy for other types of tumors, further research is essential to elucidate the specific mechanisms by which our drug delivery platform targets and damages tumors, thereby enhancing the versatility of our delivery platform.

4. Materials and methods

4.1. Chemicals and reagents

InVivoMAb anti-mouse PD-L1 (B7–H1) was obtained from BioXCell (BE0101, USA). Azide-choline (AECho) and DBCO-PEG₅-NH₂ were purchased from dianhuatech Co., Ltd (Xian, China), and Benzaldehyde-PEG₂₀₀₀-NHS was obtained from Ponsure Co., Ltd (Shanghai, China). Indocyanine green (ICG) Anhydrous sodium carbonate (Na₂CO₃, S818015) was purchased from Macklin (Shanghai, China). Potassium permanganate (KMnO₄) and other chemicals were supplied by Chuan-dong Chemical Co., Ltd (Chongqing, China). TPE-N₃ was obtained from qiyuebiology Co., Ltd (Xian, China). Dulbecco's modified Eagle medium (DMEM) was supplied by Gibco Life Technologies (Grand Island, USA). Certified fetal bovine serum (FBS) was purchased from Vivacell (Shanghai, China). 0.25 % Trypsin-EDTA solution and the CellTrace CFSE kit were obtained from Beyotime Institute of Biotechnology (Nanjing, China). Cell counting kit-8 (CCK-8) was purchased from TargetMol (Boston, USA). The antibody information used in this study was as follows: anti-arginase-1 (Arg-1) Rabbit Polyclonal antibody (Proteintech, 10661-1-AP); Anti-inducible nitric oxide synthase (iNOS) Rabbit mAb (ABclonal, A3774); anti-CD16/CD32 antibody (65057-1-Ig, Proteintech); anti-NF-κB p65 Rabbit Polyclonal antibody (Proteintech, 10745-1-AP), anti-CD86-PE (PE-65068, Proteintech); anti-CD80-FITC (FITC-65076, Proteintech); anti-CD11b-PE mAb (PE-65055, Proteintech); anti-HIF-1α antibody (Abcam, ab228649); anti-PD-L1 antibody (Abcam, ab213480).

4.2. Isolation and characterization of DC Exos

0.016 mg mL⁻¹ AECho was utilized to treat dendritic cells (DCs) [52]. The treated DCs were cultured in DMEM containing 10 % exosome-free serum for 48 h. For verification of the azide group on the membrane, DCs were stained with DBCO-Cy5.5 and analyzed by CLSM (Leica TCS SP8, Mannheim, Germany). The supernatant was then collected and subjected to differential centrifugation at 300g (10 min), 3000 g (20 min) and 10 000 g (1 h) to remove cells and debris. Finally, the supernatant was ultracentrifuged for 2 h at 120 000 g using a SorvallWX100+ (Thermo Fisher Scientific) to obtain N₃-labeled Exos. The morphology and size of Exos were evaluated by transmission electron microscopy (TEM, JEM-1200EX, Japan) and nanoparticle tracking analysis (NTA, Zeta View PMX 110, Germany), respectively. The changes in zeta potential (ξ) of the Exos with and without azide labeling were analyzed by a Mavern Zetasizer (Nano ZS90, UK). The Exo markers were analyzed via western blot.

4.3. Synthesis and characterization of anti-PD-L1-DBCO

20 μL (159 μg) of anti-PD-L1 were dissolved in 500 μL of sodium bicarbonate solution (NaHCO₃, pH = 8.5). 2 mg of Benzaldehyde-PEG₂₀₀₀-NHS ester (BD-PEG₂₀₀₀-NHS) was then added and mixed well. After the reaction at 4 °C for 4 h, the mixture was ultrafiltrated using the centrifuge tubes (Millipore Co, Amicon Ultra-0.5) at 14 000 g for 10 min to collect the product of anti-PD-L1-PEG₂₀₀₀-BD. Next, the collected product was dissolved in 500 μL of NaHCO₃ (pH = 8.5). 2 mg of dibenzocyclooctynes (DBCO)-PEG₅-NH₂ was added in the anti-PD-L1-PEG₂₀₀₀-BD solution and stirred at 4 °C for 3 h. The final product of the anti-PD-L1-PEG₂₀₀₀-DBCO was obtained by ultrafiltration centrifugation and stored in PBS buffer for future use. After the synthesis of anti-PD-L1-PEG₂₀₀₀-DBCO, typical protein peaks and peaks corresponding to alkyne and imine bonds were observed on the Raman spectrum (HORIBA, Xplora, France) [83–86]. In addition, anti-PD-L1-PEG₂₀₀₀-DBCO was further detected by azide-labeled TPE (TPE-N₃): First, TPE-N₃ was co-incubated with anti-PD-L1-PEG₂₀₀₀-DBCO, the N₃-TPE was reacted with anti-PD-L1-PEG₂₀₀₀-DBCO by click chemistry between DBCO and N₃. After the reaction was completed, the uncoupled TPE-N₃ was removed by ultrafiltration centrifuge tube to obtain the product anti-PEG₂₀₀₀-TPE. Then reaction yield was co-incubated with LLC. The fluorescent co-localization of TPE and anti-PD-L1 was observed by the CLSM which indicated the successful synthesis of anti-PD-L1-PEG₂₀₀₀-DBCO.

4.4. Preparation and characterization of ICG@MnO₂@Exo-anti-PD-L1 NPs

First, silica (SiO₂) NPs were synthesized according to the methods described in the previous literature [28]. Next, 10 mL (30 mg mL⁻¹) potassium permanganate (KMnO₄) was added dropwise into 10 mL (4 mg mL⁻¹) SiO₂ NP solution and sonicated for 6 h. The product of SiO₂ NPs coated with MnO₂ NPs were collected, and then treated with 40 mL (2 M) saturated solution of sodium carbonate (Na₂CO₃) solution at 60 °C for 12 h to obtain hollow MnO₂ NPs. Hollow MnO₂ NPs were characterized by TEM and field-emission scanning electron microscope (FE-SEM, ZeissGemini300, Germany). Similarly, Raman spectroscopy and X-ray crystal diffraction (Rigaku SmartLab SE, Japan) of MnO₂ NPs were also performed to confirm the successful preparation of the hollow MnO₂ NPs.

Next, 4 mg hollow MnO₂ NPs were mixed with 10 mL (1 mg mL⁻¹) ICG dissolved in DMSO and stirred at room temperature (700 rpm) for 24 h. The resulting mixture was then centrifuged, washed, and collected to obtain ICG-loaded MnO₂ NPs. Entrapment efficiency could be defined by the following equation: entrapment efficiency = (entrapped ICG in MnO₂ NPs)/(total ICG in stock solution) × 100 %. ICG@MnO₂ NPs were characterized by UV-Vis Spectrometer (echcomp UV-2600, China) to

suggest the loading of ICG into the hollow MnO₂ NPs. These ICG@MnO₂ NPs were then mixed with Exos and extruded through a liposome extruder (Avanti®, 610000, USA) to form ICG@MnO₂@Exo NPs. Finally, the newly synthesized anti-PD-L1-PEG₂₀₀₀-DBCO was mixed with ICG@MnO₂@Exo NPs in 500 µL of PBS for click chemistry reaction at 4 °C for 3 h. After removal of any unreacted antibodies by centrifugation (11 000 g, 20 min), the resulting product of ICG@MnO₂@Exo-anti-PD-L1 NPs was obtained and resuspended in PBS. The successful construction of ICG@MnO₂@Exo-anti-PD-L1 NPs was demonstrated by dynamic light scattering (DLS Nano Brook 90 Plus PALS) and UV-Vis spectroscopy (echcomp UV-2600, China).

4.5. The ICG@MnO₂@Exo-anti-PD-L1 NPs degradation experiment

300 µg ICG@MnO₂@Exo-anti-PD-L1 NPs were added to 2.5 mL PBS solutions with different pH (pH = 7.4 and pH = 6.5) containing 100 µM H₂O₂, and the MnO₂ absorbance at 309 nm of the solutions was measured at different time points by UV-Vis spectroscopy.

4.6. Assessment of the singlet oxygen (¹O₂) generation capacity of ICG

5 µL (10 µg µL⁻¹) 9,10-Anthracenediyl-bis (methylene) dimalonic acid (Merck, ABDA) probes were added to the 2.5 mL PBS solution containing ICG (10 µg mL⁻¹), and under irradiation with an 808 nm laser (0.5 W cm⁻²), the absorbance peaks of the solution at 300–450 nm were measured using UV-Vis spectroscopy (echcomp UV-2600, China).

4.7. Analysis of dissolved oxygen in solution

100 µM H₂O₂ was prepared using PBS buffer at pH = 7.4 and pH = 6.5, respectively. After treatment with MnO₂ or ICG@MnO₂@Exo-anti-PD-L1 NPs, the oxygen concentrations in the solution were measured. All dissolved oxygen detection experiments were measured by a dissolved oxygen meter (JPB-607A) in a 0.5 mL liquid paraffin-sealed environment.

4.8. Drug release assay of ICG@MnO₂@Exo-anti-PD-L1 NPs

Dialysis of 5 mg ICG@MnO₂@Exo-anti-PD-L1 NPs in 50 mL PBS buffer (pH = 7.4 and pH = 6.5) containing H₂O₂ was performed, and the absorbances of ICG at 780 nm in the solution at different time points were measured by UV-Vis spectroscopy.

4.9. Cell culture and cytotoxicity assay

The murine dendritic cell line (DC 2.4), the murine melanoma cell line (B16F10), the murine Lewis lung carcinoma cell line (LLC) and the murine macrophage cell line (RAW264.7) were purchased from Procell Life Science & Technology Company (Wuhan, Hubei, China). The murine pulmonary epithelial cell line (MLE-12) was obtained from the WheLab (Shanghai, China). B16F10 and RAW264.7 cells were cultured in RPMI 1640 medium. MLE-12 cells were cultured in a proprietary medium (M1025A, WheLab). In addition, LLC cells and DC 2.4 cells were cultured in DMEM. All medium was supplemented with 10 % (v/v) fetal bovine serum (FBS) and 1 % (v/v) antibiotics (penicillin-streptomycin). The cytotoxicity of ICG@MnO₂@Exo-anti-PD-L1 NPs was evaluated using CCK8 assays. First, 1 × 10⁴ LLC cells were seeded in a 96-well plate. Upon reaching a confluency of 70 %, the cells were incubated with PBS, ICG, ICG@MnO₂, ICG@MnO₂@Exo, ICG@MnO₂@Exo-anti-PD-L1 (0, 1, 1.5, 2.5 and 3 µg mL⁻¹) for 24 h. The concentrations of the treatments were quantified by the ICG concentration. Finally, the cells were further incubated with the fresh culture medium containing 10 % CCK8 solution for 30 min, and cell viability was measured by a microplate reader (Tecan; Infinite F50, Switzerland) at 450 nm.

4.10. Cellular uptake assay

LLC cells were seeded in a 6-well plate, and then ICG@MnO₂@Exo-anti-PD-L1 NPs were added at 2 µg mL⁻¹ in DMEM. At different time points after adding NPs (0, 1, 2, 4, 6, 8, and 10 h), cells were collected and subjected to flow cytometry to detect the fluorescence intensity of ICG in the cells.

4.11. Hypoxia evaluation in LLC

LLC cells were seeded in a 24-well plate containing slides and grown on the cover slide for 6 h under hypoxia (1 % O₂). The cells were then treated with PBS, ICG, ICG@MnO₂, ICG@MnO₂@Exo and ICG@MnO₂@Exo-anti-PD-L1 at 2 µg mL⁻¹, respectively, and continued to be cultured under hypoxia condition for 12 h. The HIF-1α expression levels in different treatment groups were detected by western blot.

4.12. Western blot

Cells were lysed in cell lysis buffer (pH = 7.5, 20 mM Tris, 150 mM NaCl, 1 % Triton X-100, Beyotime Biotechnology) with protease inhibitors (phenylmethanesulfonyl fluoride, PMSF, Beyotime Biotechnology) at a ratio of 100:1 (4 °C, 30 min), followed by centrifugation at 12 000 rpm for 15 min. After adding 5 × sample loading buffer (v/v = 4:1), proteins were fully denatured by boiling (100 °C, 10 min). The proteins were separated by sodium dodecyl-sulfate polyacrylamide gel electrophoresis (SDS-PAGE) and the electrophoresis time was adjusted based on the molecular weight of the target proteins and the concentration of the SDS gel. The proteins were then transferred to a polyvinylidene difluoride (PVDF) membrane for 60–180 min at 250 mA. The PVDF membrane was then blocked with 1 × Tris-buffered saline containing 1 % Tween 20 (TBST) buffer with 5 % bovine serum albumin (BSA). The PVDF membrane was incubated with primary antibodies (1:1000 dilution) at 4 °C overnight, and washed with TBST for 3 times (5 min/time). Next, the PVDF membrane was incubated with horseradish peroxidase (HRP)-conjugated goat anti-rabbit or goat anti-mouse secondary antibody (1:2000 dilution) in 1 × TBST buffer at room temperature with shaking for 1 h. β-actin or GAPDH was used as the loading control. The expression levels of proteins were assessed via Enhanced Chemiluminescence Detection System (ECL, Proteintech, USA).

4.13. Laser scanning confocal microscopy imaging

FRAP: Exosomes were labeled with DIO dye, co-incubated with live cells, and the fluorescence in the specific position was quenched by laser under a laser confocal microscope to observe whether the fluorescence in the quenched area would increase with time.

RAW264.7 cells were cultured in a 24-well plate with the treatments of PBS, ICG, ICG@MnO₂, ICG@MnO₂@Exo and ICG@MnO₂@Exo-anti-PD-L1 (2 µg mL⁻¹) and grown on the cover slide for 24 h. The cells were fixed with 4 % paraformaldehyde for 15 min and then blocked by 5 % BSA for 1 h at room temperature. These RAW264.7 cells were then incubated with specific fluorescent antibodies (CD11b-PE and CD80-FITC, diluted 1:100, Proteintech) at 4 °C for 2 h, respectively. The nuclei were stained with DAPI for 30 min at room temperature. Subsequently, DAPI (blue), FITC (green), and PE (red) signals were observed using the Leica TCS SP8 confocal laser scanning microscope.

To examine the expression of HIF-1α, PD-L1, and immune-related cell markers in tumor tissues, the tumor tissues were collected after different treatments for 48 h and labeled for HIF-1α and PD-L1. On the 16 days after treatment, tumor tissues were collected and the expression of macrophage markers (F4/80, CD86, and CD206) and T cell markers (Foxp3, CD4, and CD8) were detected. Briefly, tissue sections were blocked with 3 % BSA blocking buffer, followed by incubation with primary antibodies for 12 h at 4 °C. The corresponding secondary antibodies conjugated with Alexa Fluor® 488 or Alexa Fluor® 594 were

then added and incubated for 1 h at 37 °C. Moreover, tumor tissue sections were stained for TUNEL according to the manufacturer's instructions.

4.14. Cellular phagocytosis of cancer cells by reprogrammed macrophages

LLC cells were stained with the CFDA SE Cell Proliferation and Tracer Kit (C0051, Beyotime Biotechnology) according to the instructions and cultured for 24 h. At the same time, macrophages were induced with 100 ng/mL IL-4 for 24 h to obtain M2 macrophages. Then LLC cells were collected and co-cultured with M2 macrophages (LLC: M2 = 4:1) on a 24-well plate and grown on the slides for an additional 24 h. At the same time, PBS, ICG, ICG@MnO₂, ICG@MnO₂@Exo and ICG@MnO₂@Exo-anti-PD-L1 NPs (2 μg mL⁻¹) were added to the culture medium, respectively. The cells were fixed with 4 % paraformaldehyde for 15 min, stained with anti-mouse CD11b-PE antibody and analyzed by CLSM.

4.15. Flow cytometry

1 × 10⁶ M2 macrophages were seeded in a 6-well plate and grown to 70 % confluence. After 24 h of treatment with PBS, ICG, ICG@MnO₂, ICG@MnO₂@Exo and ICG@MnO₂@Exo-anti-PD-L1 NPs (2 μg mL⁻¹), the cells were collected by centrifugation at 350g (4 °C, 5 min). CD16/32 antibodies (65057-1-ig, Proteintech) diluted in flow cytometry staining buffer were added as the blocking agent for 25 min. The cells were then stained with CD80-FITC (FITC-65076, Proteintech) and CD86-PE (PE-65068, Proteintech) for 30 min. The cells were washed twice and analyzed by BD FACSCelesta™.

4.16. Assessment of the intracellular PDT effect of ICG@MnO₂@Exo-anti-PD-L1 NPs

A commercial ¹O₂ assay kit, Singlet Oxygen Sensor Green (SOSG), was used to investigate the ICG@MnO₂@Exo-anti-PD-L1 NPs-enhanced ¹O₂ generation. LLC cells were cultured under low oxygen (1 % O₂) conditions throughout the assay. When the confluence reached 70 % on glass slides in a 24-well plate, they were co-incubated with PBS, ICG, ICG@MnO₂, ICG@MnO₂@Exo and ICG@MnO₂@Exo-anti-PD-L1 NPs (2 mg mL⁻¹) for 4 h. The cell culture medium was then removed and the cells were washed once with PBS. DMEM containing 100 μM SOSG was added to the 24-well plate and incubated for 2 h. The cells were then exposed to 808 nm laser irradiation for 10 min at the power density of 0.5 W cm⁻². Finally, the production of singlet oxygen in each group was observed under the CLSM.

4.17. ELISA detection of tumor immunogenic cell death (ICD) and macrophage markers

LLC cells and M2 macrophages were co-cultured in a 6-well plate of transwell system at a ratio of 4:1. After the cells reached 70 % confluence, LLC were treated with PBS, ICG, ICG@MnO₂, ICG@MnO₂@Exo and ICG@MnO₂@Exo-anti-PD-L1 NPs (2 μg mL⁻¹) prepared in cell culture medium for 24 h. The cell supernatant was collected by centrifugation (1000 g, 10 min, 4 °C) and analyzed using ELISA assay kits to detect the expression levels of the cytokines including IL-10, TNF-α, and HMGB-1. The ELISA was performed according to the protocol of Quanzhou Jiubang Biotechnology Co., Ltd.

4.18. Assessments of pathological morphology

Hematoxylin & Eosin (H&E) staining was used to visualize the morphology of the major organs and tumors in mice. H&E staining was performed according to the previously reported method [87] and analyzed under a microscope (Nexcope NIB410, USA).

4.19. Immunohistochemistry

Preceding Ki-67 staining, slides underwent antigen retrieval consisting of incubation in sodium citrate buffer (10 mM Sodium Citrate, 0.05 % Tween 20, pH = 6.0) at 85 °C for 20 min. Tumor sections were then blocked with a 0.25 % (v/v) Triton X-100 and 5 % (v/v) goat serum PBS solution and then incubated with anti-Ki-67 antibody overnight at 4 °C. Species-specific HRP-conjugated secondary antibody were then applied for 20 min at room temperature.

4.20. Animal experiments

Male C57BL/6 mice (8-week-old) were purchased from Animal Center of Chongqing Medical University. The tumor-bearing mouse model was constructed by subcutaneous injection of LLC cells (1 × 10⁶ cells in 200 μL PBS) to dorsal skinfold chamber, and when the tumor volume reached 100 mm³ (V = length × width²/2), the mice divided into 6 groups (PBS, PBS + L, ICG + L, ICG@MnO₂+L, ICG@MnO₂@Exo + L, ICG@MnO₂@Exo-anti-PD-L1+L) and performed the corresponding treatments. Except for the PBS group, the dosage for the remaining groups was calculated based on a ratio of ICG (3 mg kg⁻¹). Fluorescent images of mice were obtained using the LB983 NightOWL II imaging system at 2, 4, 6, 8, 12 and 24 h after injection. At 4 h after tail vein injection, under general anesthesia (1 % pentobarbital sodium, 45 mg kg⁻¹ intraperitoneal injection), the tumor was treated with 808 nm laser with 0.5 W cm⁻² for 10 min. After treatment tumor size and mouse weight were recorded every two days starting from the first day of treatment. In addition, serum and blood samples were collected from the mice on day 9. After 16 days, the mice were sacrificed and the main organs were harvested for H&E to evaluate the biological safety of the NPs and the mouse lung tissues were collected to evaluate tumor lung metastasis. TUNEL and Ki-67 staining were performed on the mouse tumors. In addition, the mouse tumors were also collected for immunofluorescence staining to assess the distribution of immune cells and the expression of hypoxia-related markers. In addition, mice were irradiated and sacrificed at 1 h after tail vein injection of pimonidazole, and mouse tumors were harvested for frozen section to analyze hypoxia. Singlet oxygen production during PDT was assessed by injecting 50 μL SOSG (25 μM) through the tail vein at 1 h in advance and the tumors were collected for frozen section to detect the fluorescence intensity of SOSG.

4.21. Statistical analysis

All the experiments were independently repeated at least three times, and the data were presented as mean ± standard deviation (SD). The significance of all experimental data was determined using Student's t-test and One-way single factorial analysis of variance (ANOVA), and the statistical significance of p-values was denoted as * < 0.05, ** < 0.01, *** < 0.001, and **** < 0.0001, ns: no significance, respectively.

Ethics approval statement

The study was approved by the Ethics Committee of Chongqing Medical University (Chongqing, China). All animal experiments were conducted in accordance with the Guidelines for the Care and Use of Laboratory Animals.

Funding

This work was supported by National Natural Science Foundation of China (Grant No. 82203310 and No. 81972023); Natural Science Foundation of Chongqing City (Grant No. CSTC2021jcyj-msxm0172 and CSTC2022nscq-msx0054); Science and Technology Research Program of Chongqing Municipal Education Commission (Grant No. KJQN202300478); Creative Research Group of CQ University (Grant

No. CXQT21017) and Program for Youth Innovation in Future Medicine from Chongqing Medical University.

Data and materials availability

All data needed to evaluate the conclusions in the paper are present in the paper and/or the Supplementary Materials. Additional data related to this paper may be requested from the authors.

Ethics approval and consent to participate

The study was approved by the Ethics Committee of Chongqing Medical University (Chongqing, China). All animal experiments were conducted in accordance with the Guidelines for the Care and Use of Laboratory Animals.

CRedit authorship contribution statement

Jiao Guo: Writing – original draft, Methodology. **Wei Zhao:** Writing – original draft, Methodology. **Xinyu Xiao:** Methodology. **Shanshan Liu:** Validation. **Liang Liu:** Validation. **La Zhang:** Visualization. **Lu Li:** Visualization. **Zhenghang Li:** Visualization. **Zhi Li:** Validation. **Mengxia Xu:** Validation. **Qiling Peng:** Writing – review & editing, Funding acquisition. **Jianwei Wang:** Writing – review & editing, Funding acquisition. **Yuxian Wei:** Writing – review & editing, Funding acquisition. **Ning Jiang:** Writing – review & editing, Funding acquisition.

Declaration of competing interest

The authors declare no competing interest.

Acknowledgments

We gratefully thank the Molecular Medicine and Cancer Research Center of Chongqing Medical University for the excellent technical assistance at the confocal microscope.

Appendix A. Supplementary data

Supplementary data to this article can be found online at <https://doi.org/10.1016/j.bioactmat.2024.05.030>.

References

- [1] H. Sung, et al., Global cancer Statistics 2020: GLOBOCAN estimates of incidence and mortality worldwide for 36 cancers in 185 countries, *CA A Cancer J. Clin.* 71 (2021) 209–249.
- [2] W. Xue, et al., Response and resistance to NF- κ B inhibitors in mouse models of lung adenocarcinoma, *Cancer Discov.* 1 (2011) 236–247.
- [3] H. Tang, et al., Comprehensive evaluation of published gene expression prognostic signatures for biomarker-based lung cancer clinical studies, *Ann. Oncol.* 28 (2017) 733–740.
- [4] S.S. Dhillon, et al., A phase I study of light dose for photodynamic therapy using 2-[1-hexyloxyethyl]-2 devinyl pyropheophorbide-a for the treatment of non-small cell carcinoma in situ or non-small cell microinvasive bronchogenic carcinoma: a dose ranging study, *J. Thorac. Oncol.* 11 (2016) 234–241.
- [5] S.S. Ramalingam, T.K. Owonikoko, F.R. Khuri, Lung cancer: new biological insights and recent therapeutic advances, *CA A Cancer J. Clin.* 61 (2011) 91–112.
- [6] L. Galluzzi, T.A. Chan, G. Kroemer, J.D. Wolchok, A. López-Soto, The hallmarks of successful anticancer immunotherapy, *Sci. Transl. Med.* 10 (2018).
- [7] A.Y. Chen, J.D. Wolchok, A.R. Bass, TNF in the era of immune checkpoint inhibitors: friend or foe? *Nat. Rev. Rheumatol.* 17 (2021) 213–223.
- [8] E. Ziv, et al., Lung adenocarcinoma: predictive value of KRAS mutation status in assessing local recurrence in patients undergoing image-guided ablation, *Radiology* 282 (2017) 251–258.
- [9] S.E. Witta, et al., Randomized phase II trial of erlotinib with and without entinostat in patients with advanced non-small-cell lung cancer who progressed on prior chemotherapy, *J. Clin. Oncol.* 30 (2012) 2248–2255.
- [10] E.S. Kim, et al., Tissue platinum concentration and tumor response in non-small-cell lung cancer, *J. Clin. Oncol.* 30 (2012) 3345–3352.
- [11] J. Wang, et al., BRD4-IRF1 axis regulates chemoradiotherapy-induced PD-L1 expression and immune evasion in non-small cell lung cancer, *Clin. Transl. Med.* 12 (2022) e718.
- [12] N. Vasan, J. Baselga, D.M. Hyman, A view on drug resistance in cancer, *Nature* 575 (2019) 299–309.
- [13] A. Marusyk, M. Janiszewska, K. Polyak, Intratumor heterogeneity: the rosetta stone of therapy resistance, *Cancer Cell* 37 (2020) 471–484.
- [14] X. Hu, et al., Emerging photodynamic/sonodynamic therapies for urological cancers: progress and challenges, *J. Nanobiotechnol.* 20 (2022) 437.
- [15] X. Gu, et al., CuS nanoparticles as a photodynamic nanoswitch for abrogating bypass signaling to overcome gefitinib resistance, *Nano Lett.* 19 (2019) 3344–3352.
- [16] Y. Zhang, et al., A novel multi-functionalized multicellular nanodelivery system for non-small cell lung cancer photochemotherapy, *J. Nanobiotechnol.* 19 (2021) 245.
- [17] M. Liu, et al., Crosslinked self-assembled nanoparticles for chemo-sonodynamic combination therapy favoring antitumor, antimetastasis management and immune responses, *J. Contr. Release* 290 (2018) 150–164.
- [18] J.D. Gordan, J.A. Bertout, C.J. Hu, J.A. Diehl, M.C. Simon, HIF-2 α promotes hypoxic cell proliferation by enhancing c-myc transcriptional activity, *Cancer Cell* 11 (2007) 335–347.
- [19] D. Zhu, J. Zhang, G. Luo, Y. Duo, B.Z. Tang, Bright bacterium for hypoxia-tolerant photodynamic therapy against orthotopic colon tumors by an interventional method, *Adv. Sci.* 8 (2021) e2004769.
- [20] G. Yang, et al., Hollow MnO₂ as a tumor-microenvironment-responsive biodegradable nano-platform for combination therapy favoring antitumor immune responses, *Nat. Commun.* 8 (2017) 902.
- [21] L. Yu, et al., "Manganese extraction" strategy enables tumor-sensitive biodegradability and theranostics of nanoparticles, *J. Am. Chem. Soc.* 138 (2016) 9881–9894.
- [22] L.S. Lin, et al., Simultaneous fenton-like ion delivery and glutathione depletion by MnO₂-based nanoagent to enhance chemodynamic therapy, *Angew. Chem. Int. Ed. Engl.* 57 (2018) 4902–4906.
- [23] Z. Shen, et al., Tumor microenvironment-triggered nanosystems as dual-relief tumor hypoxia immunomodulators for enhanced phototherapy, *Theranostics* 10 (2020) 9132–9152.
- [24] M. Yu, et al., Multifunctional nanoregulator reshapes immune microenvironment and enhances immune memory for tumor immunotherapy, *Adv. Sci.* 6 (2019) 1900037.
- [25] M. Song, T. Liu, C. Shi, X. Zhang, X. Chen, Bioconjugated manganese dioxide nanoparticles enhance chemotherapy response by priming tumor-associated macrophages toward M1-like phenotype and attenuating tumor hypoxia, *ACS Nano* 10 (2016) 633–647.
- [26] E.M. Scott, et al., Bi- and tri-valent T cell engagers deplete tumour-associated macrophages in cancer patient samples, *J. Immunot. Cancer* 7 (2019) 320.
- [27] S.M. Horwitz, et al., Activity of the PI3K- δ , γ inhibitor duvelisib in a phase 1 trial and preclinical models of T-cell lymphoma, *Blood* 131 (2018) 888–898.
- [28] F. Gao, et al., Intra/Extracellular lactic acid exhaustion for synergistic metabolic therapy and immunotherapy of tumors, *Adv. Mater.* 31 (2019) e1904639.
- [29] Z. Wang, et al., Biomimetic nanoflowers by self-assembly of nanozymes to induce intracellular oxidative damage against hypoxic tumors, *Nat. Commun.* 9 (2018) 3334.
- [30] Z. Zhou, et al., Metabolic reprogramming mediated PD-L1 depression and hypoxia reversion to reactivate tumor therapy, *J. Contr. Release* 352 (2022) 793–812.
- [31] H. Maeda, H. Nakamura, J. Fang, The EPR effect for macromolecular drug delivery to solid tumors: improvement of tumor uptake, lowering of systemic toxicity, and distinct tumor imaging in vivo, *Adv. Drug Deliv. Rev.* 65 (2013) 71–79.
- [32] A.P. Castano, P. Mroz, M.R. Hamblin, Photodynamic therapy and anti-tumour immunity, *Nat. Rev. Cancer* 6 (2006) 535–545.
- [33] X. Zhao, J. Liu, J. Fan, H. Chao, X. Peng, Recent progress in photosensitizers for overcoming the challenges of photodynamic therapy: from molecular design to application, *Chem. Soc. Rev.* 50 (2021) 4185–4219.
- [34] J. Chen, et al., Tumor extracellular vesicles mediate anti-PD-L1 therapy resistance by decoying anti-PD-L1, *Cell. Mol. Immunol.* 19 (2022) 1290–1301.
- [35] X. Wang, et al., PD-L1 is a direct target of cancer-FOXP3 in pancreatic ductal adenocarcinoma (PDAC), and combined immunotherapy with antibodies against PD-L1 and CCL5 is effective in the treatment of PDAC, *Signal Transduct. Targeted Ther.* 5 (2020) 38.
- [36] G.J. Freeman, et al., Engagement of the PD-1 immunoinhibitory receptor by a novel B7 family member leads to negative regulation of lymphocyte activation, *J. Exp. Med.* 192 (2000) 1027–1034.
- [37] J. Yu, et al., Regulation of sister chromatid cohesion by nuclear PD-L1, *Cell Res.* 30 (2020) 590–601.
- [38] Q. Huang, et al., Impact of PD-L1 expression, driver mutations and clinical characteristics on survival after anti-PD-1/PD-L1 immunotherapy versus chemotherapy in non-small-cell lung cancer: a meta-analysis of randomized trials, *Oncolimmunology* 7 (2018) e1396403.
- [39] D. Wang, et al., Immunogenic chemotherapy effectively inhibits KRAS-Driven lung cancer, *Cancer Lett.* 492 (2020) 31–43.
- [40] X. Cao, et al., m(6)A methylation: a process reshaping the tumour immune microenvironment and regulating immune evasion, *Mol. Cancer* 22 (2023) 42.
- [41] R. Yang, et al., Charge and size dual switchable nanocage for novel triple-interlocked combination therapy pattern, *Adv. Sci.* 7 (2020) 2000906.
- [42] Y. Cao, et al., Glucocorticoid receptor translational isoforms underlie maturational stage-specific glucocorticoid sensitivities of dendritic cells in mice and humans, *Blood* 121 (2013) 1553–1562.

- [43] M. Liu, S. Hu, N. Yan, K.D. Popowski, K. Cheng, Inhalable extracellular vesicle delivery of IL-12 mRNA to treat lung cancer and promote systemic immunity, *Nat. Nanotechnol.* 19 (2024) 565–575.
- [44] W. Xu, Z. Yang, N. Lu, From pathogenesis to clinical application: insights into exosomes as transfer vectors in cancer, *J. Exp. Clin. Cancer Res.* 35 (2016) 156.
- [45] Z. Hu, et al., Ultrafine MnO₂ nanoparticles decorated on graphene oxide as a highly efficient and recyclable catalyst for aerobic oxidation of benzyl alcohol, *J. Colloid Interface Sci.* 483 (2016) 26–33.
- [46] A.V. Soldatova, et al., Biogenic and synthetic MnO(2) nanoparticles: size and growth probed with absorption and Raman spectroscopies and dynamic light scattering, *Environ. Sci. Technol.* 53 (2019) 4185–4197.
- [47] W. Zhang, M. Liu, A. Liu, G. Zhai, Advances in functionalized mesoporous silica nanoparticles for tumor targeted drug delivery and theranostics, *Curr. Pharmaceut. Des.* 23 (2017) 3367–3382.
- [48] M. Vallet-Regí, F. Schüth, D. Lozano, M. Colilla, M. Manzano, Engineering mesoporous silica nanoparticles for drug delivery: where are we after two decades? *Chem. Soc. Rev.* 51 (2022) 5365–5451.
- [49] W. Holzer, et al., Photostability and thermal stability of indocyanine green, *J. Photochem. Photobiol., B* 47 (1998) 155–164.
- [50] Z. Wang, et al., Exosomes decorated with a recombinant SARS-CoV-2 receptor-binding domain as an inhalable COVID-19 vaccine, *Nat. Biomed. Eng.* 6 (2022) 791–805.
- [51] I. Nilsson, et al., Metabolic phospholipid labeling of intact bacteria enables a fluorescence assay that detects compromised outer membranes, *J. Lipid Res.* 61 (2020) 870–883.
- [52] T. Tamura, et al., Organelle membrane-specific chemical labeling and dynamic imaging in living cells, *Nat. Chem. Biol.* 16 (2020) 1361–1367.
- [53] W. Nie, et al., Responsive exosome nano-bioconjugates for synergistic cancer therapy, *Angew Chem. Int. Ed. Engl.* 59 (2020) 2018–2022.
- [54] S.A. Oladepo, et al., UV resonance Raman investigations of peptide and protein structure and dynamics, *Chem. Rev.* 112 (2012) 2604–2628.
- [55] N. Félijd, et al., Optimized surface-enhanced Raman scattering on gold nanoparticle arrays, *Appl. Phys. Lett.* 82 (2003) 3095–3097.
- [56] W.J. Tipping, M. Lee, A. Serrrels, V.G. Brunton, A.N. Hulme, Stimulated Raman scattering microscopy: an emerging tool for drug discovery, *Chem. Soc. Rev.* 45 (2016) 2075–2089.
- [57] G. Eyring, R. Mathies, Resonance Raman studies of bathorhodopsin: evidence for a protonated Schiff base linkage, *Proc. Natl. Acad. Sci. U. S. A.* 76 (1979) 33–37.
- [58] R. Resmi, J. Parvathy, A. John, R. Joseph, Injectable self-crosslinking hydrogels for meniscal repair: a study with oxidized alginate and gelatin, *Carbohydr. Polym.* 234 (2020) 115902.
- [59] K. Cheng, R. Kalluri, Guidelines for clinical translation and commercialization of extracellular vesicles and exosomes based therapeutics, *Extracell. Vesicle* 2 (2023) 100029.
- [60] J.S. Suk, Q. Xu, N. Kim, J. Hanes, L.M. Ensign, PEGylation as a strategy for improving nanoparticle-based drug and gene delivery, *Adv. Drug Deliv. Rev.* 99 (2016) 28–51.
- [61] F. Pi, et al., Alleviating the hypoxic tumor microenvironment with MnO(2)-coated CeO(2) nanoplatform for magnetic resonance imaging guided radiotherapy, *J. Nanobiotechnol.* 21 (2023) 90.
- [62] Q. Chen, et al., Intelligent albumin-MnO₂ nanoparticles as pH-/H₂O₂-responsive dissociable nanocarriers to modulate tumor hypoxia for effective combination therapy, *Adv. Mater.* 28 (2016) 7129–7136.
- [63] G.L. Semenza, Targeting HIF-1 for cancer therapy, *Nat. Rev. Cancer* 3 (2003) 721–732.
- [64] J. Liu, et al., Parkin targets HIF-1 α for ubiquitination and degradation to inhibit breast tumor progression, *Nat. Commun.* 8 (2017) 1823.
- [65] M.Z. Noman, et al., PD-L1 is a novel direct target of HIF-1 α , and its blockade under hypoxia enhanced MDSC-mediated T cell activation, *J. Exp. Med.* 211 (2014) 781–790.
- [66] B. Xu, et al., Immunomodulation-enhanced nanozyme-based tumor catalytic therapy, *Adv. Mater.* 32 (2020) e2003563.
- [67] M. Lv, et al., Manganese is critical for antitumor immune responses via cGAS-STING and improves the efficacy of clinical immunotherapy, *Cell Res.* 30 (2020) 966–979.
- [68] X. Sun, et al., Amplifying STING activation by cyclic dinucleotide-manganese particles for local and systemic cancer metalloimmunotherapy, *Nat. Nanotechnol.* 16 (2021) 1260–1270.
- [69] S.K. Biswas, A. Mantovani, Macrophage plasticity and interaction with lymphocyte subsets: cancer as a paradigm, *Nat. Immunol.* 11 (2010) 889–896.
- [70] H.S. Choi, et al., Renal clearance of quantum dots, *Nat. Biotechnol.* 25 (2007) 1165–1170.
- [71] A.K. Kirchherr, A. Briel, K. Mäder, Stabilization of indocyanine green by encapsulation within micellar systems, *Mol. Pharm.* 6 (2009) 480–491.
- [72] M. Liu, et al., Redox/enzyme sensitive chondroitin sulfate-based self-assembled nanoparticles loading docetaxel for the inhibition of metastasis and growth of melanoma, *Carbohydr. Polym.* 184 (2018) 82–93.
- [73] H. Xu, et al., Nano-puerarin regulates tumor microenvironment and facilitates chemo- and immunotherapy in murine triple negative breast cancer model, *Biomaterials* 235 (2020) 119769.
- [74] D. Wang, et al., Self-assembled single-atom nanozyme for enhanced photodynamic therapy treatment of tumor, *Nat. Commun.* 11 (2020) 357.
- [75] S. Hu-Lieskovan, et al., SITC cancer immunotherapy resource document: a compass in the land of biomarker discovery, *J. Immunot. Cancer* 8 (2020).
- [76] M.A. Lakin, E. Ghorani, H. Munir, C.P. Martins, J.D. Shields, Cancer-associated fibroblasts induce antigen-specific deletion of CD8 (+) T Cells to protect tumour cells, *Nat. Commun.* 9 (2018) 948.
- [77] E. Allen, et al., Combined antiangiogenic and anti-PD-L1 therapy stimulates tumor immunity through HEV formation, *Sci. Transl. Med.* 9 (2017).
- [78] N. Duma, R. Santana-Davila, J.R. Molina, Non-small cell lung cancer: epidemiology, screening, diagnosis, and treatment, *Mayo Clin. Proc.* 94 (2019) 1623–1640.
- [79] H. Chen, et al., Gadolinium-encapsulated graphene carbon nanotheranostics for imaging-guided photodynamic therapy, *Adv. Mater.* (2018) e1802748.
- [80] D. Wu, et al., Efficacy-shaping nanomedicine by loading calcium peroxide into tumor microenvironment-responsive nanoparticles for the antitumor therapy of prostate cancer, *Theranostics* 10 (2020) 9808–9829.
- [81] S. Wang, et al., Metabolic intervention liposome boosted lung cancer radio-immunotherapy via hypoxia amelioration and PD-L1 restraint, *Adv. Sci.* 10 (2023) e2207608.
- [82] Y. Liu, et al., Tumor selective metabolic reprogramming as a prospective PD-L1 depression strategy to reactivate immunotherapy, *Adv. Mater.* 34 (2022) e2206121.
- [83] G. Pezzotti, et al., Raman molecular fingerprints of SARS-CoV-2 British variant and the concept of Raman barcode, *Adv. Sci.* 9 (2022) e2103287.
- [84] L. Wei, et al., Live-cell bioorthogonal chemical imaging: stimulated Raman scattering microscopy of vibrational probes, *Acc. Chem. Res.* 49 (2016) 1494–1502.
- [85] M. Sulkes, A. Lewis, A.T. Lemley, R. Cookingham, Modeling the resonance Raman spectrum of a metarhodopsin: implications for the color of visual pigments, *Proc. Natl. Acad. Sci. U. S. A.* 73 (1976) 4266–4270.
- [86] G. Xu, et al., An ultrasensitive surface-enhanced Raman scattering sensor for the detection of hydrazine via the Schiff base reaction, *J. Hazard Mater.* 424 (2022) 127303.
- [87] R.N. Judson, et al., Inhibition of methyltransferase Setd7 allows the in vitro expansion of myogenic stem cells with improved therapeutic potential, *Cell Stem Cell* 22 (2018) 177–190.e177.